

## Research Paper

CO<sub>2</sub> retrievals in the Mars daylight thermosphere from its 4.3 μm limb emission measured by OMEGA/MEx

Sergio Jiménez-Monferrer <sup>a,\*</sup>, Miguel Ángel López-Valverde <sup>a</sup>, Bernd Funke <sup>a</sup>, Francisco González-Galindo <sup>a</sup>, Arianna Piccialli <sup>b</sup>, Maya García-Comas <sup>a</sup>, Manuel López-Puertas <sup>a</sup>, Brigitte Gondet <sup>c</sup>, Jean-Pierre Bibring <sup>c</sup>

<sup>a</sup> IAA-CSIC, Glorieta de la Astronomía, s/n, 18008 Granada, Spain

<sup>b</sup> BIRA-IASB, Ringlaan-3 Avenue Circulaire, B-1180 Brussels, Belgium

<sup>c</sup> CNRS, Université Paris-Sud, Institut d'Astrophysique Spatiale (IAS), 91405 Orsay, France

## ARTICLE INFO

**Keywords:**  
Mars atmosphere  
Remote-sensing  
CO<sub>2</sub>  
Retrieval scheme  
Non-LTE  
OMEGA

## ABSTRACT

We present a non-local thermodynamic equilibrium retrieval scheme for atmospheric composition and its application to Mars CO<sub>2</sub> infrared limb emissions as measured by the OMEGA instrument on board Mars Express (MEx). These emissions are caused by CO<sub>2</sub> fluorescence of solar radiation, and thus the retrieval scheme accounts for non-LTE processes. We analyzed the dayside limb observations from a selection of three OMEGA orbits or data *gubes*. Before the retrieval was applied, we performed a radiometric calibration, cleaned the spectra (including clustering techniques) and generated radiance vertical profiles for each dataset. We also present information on the inversion set up, results on the retrieved CO<sub>2</sub> density profiles, as well as the temperature profiles derived from the CO<sub>2</sub> densities by assuming hydrostatic equilibrium. An extensive sensitivity study of the retrieval scheme was carried out, including its application to the OMEGA spectra taken at different MEx orbital configurations, to conclude on its performance and to offer recommendations for its systematic use with MEx datasets. The uncertainty due to the instrumental Gain calibration and that caused by the retrieval noise error itself are of large importance for the inversion, but a comparable component of the total error comes from the uncertainties of the temperature provided by the GCM. We demonstrated that, between 120 and 160 km, CO<sub>2</sub> profiles can be derived with a precision around 30% and a vertical resolution of about 15 km.

## 1. Introduction

Several instruments on board Mars Express (MEx) have observed strong daytime atmospheric emissions in the infrared, originated at high altitudes (above 50 km) in the Martian atmosphere. This is the case of the emissions observed by OMEGA and PFS, two instruments on board MEx, in the spectral range around 4.3 μm (Formisano et al., 2006; López-Valverde et al., 2011; Piccialli et al., 2016). Due to solar fluorescent emissions of CO<sub>2</sub>, these datasets have not been sufficiently exploited so far, although if non-local thermodynamic effects were properly accounted for, both temperature and CO<sub>2</sub> density could be retrieved from them.

Non-LTE retrievals of CO and CO<sub>2</sub> from IR emissions at high altitudes have been undertaken in the case of the Earth atmosphere (Jurado-Navarro et al., 2016; Funke et al., 2009; Kaufmann et al., 2002; Mertens

et al., 2009), and were recently performed for Titan's (Adriani et al., 2011; García-Comas et al., 2011) and Venus' (Gilli et al., 2015; Peralta et al., 2016) atmospheres. The retrievals on Venus were performed for CO from VIRTIS/Venus Express measurements, assuming optically thin conditions, or from a nadir down-looking geometry, with a fixed and broad emission layer, which simplifies the inversion. On Earth, CO<sub>2</sub> is a minor species, unlike the case of Mars. The application of a non-LTE retrieval in a limb geometry which addresses optically thin and thick conditions and from the emission of the dominant species of the atmosphere is an entirely new problem in terrestrial atmospheres.

CO<sub>2</sub> contains strong ro-vibrational bands, which can absorb enough solar energy in the near IR to produce a significant pumping of some of their vibrational states. Sophisticated non-LTE models for the Martian atmosphere were developed in the last decades with the purpose of analyzing the non-LTE emission measurements and for including non-

\* Corresponding author.

E-mail address: [sergio.jimenez@uv.es](mailto:sergio.jimenez@uv.es) (S. Jiménez-Monferrer).

LTE cooling/heating rates in atmospheric GCMs (Stepanova and Shved, 1985; López-Valverde et al., 2011). These models show that the absorption of IR solar radiation excites CO<sub>2</sub> vibrational levels that relax either re-emitting in the same wavelengths (fluorescence) or by collisional cascades to lower levels, where they emit photons in different bands in the 4.3 μm region (indirect solar fluorescence) (López-Valverde and López-Puertas, 1994a).

These fluorescent emission have been studied before by Piccialli et al. (2016). They reported three Martian years of observations of CO<sub>2</sub> non-LTE limb emissions with OMEGA and studied their altitude variation from the spectral images. They found that the thermal structure (affecting the tangent altitude of the peak emission) and the solar illumination conditions (affecting the intensity of the emission) are the two parameters mainly influencing the observed emission, and obtained a good agreement with the non-LTE model used in their work, that of López-Valverde and López-Puertas (1994a). The main difference between the data and the model they found is in the spectral region of 4.38 – 4.48 μm, where the observed intensity was larger than that predicted by the model. They also obtained a variation of the peak emission with atmospheric conditions, while the pressure level of the emission peak remained approximately constant at  $\sim 0.03 \pm 0.01$  Pa, in consonance with model simulations. These CO<sub>2</sub> non-LTE limb emissions, however, have not been used so far to retrieve density or temperature in the Martian atmosphere.

Both OMEGA and PFS provide a comprehensive dataset of these emissions. OMEGA provides simultaneous imaging and spectra of the CO<sub>2</sub> emissions with a relatively small field of view, allowing studying the altitude variation of the 4.3 μm emission (Piccialli et al., 2016). On the other hand, PFS has a larger field of view, but a better spectral resolution. This work focuses on the OMEGA dataset.

This work aims at the retrieval of CO<sub>2</sub> densities in the upper atmosphere of Mars (120–200 km) from daytime observations in the 4.3 μm region in the limb of the planet. We combined state-of-the-art non-LTE models and line-by-line retrieval techniques. From the retrieved density profiles of CO<sub>2</sub> we then derived temperature profiles assuming hydrostatic equilibrium.

### 1.1. Outline

Section 2 explores the content of a typical OMEGA *qube* and details the generation of calibrated limb spectra from non-calibrated level 0 data. Section 3 describes the non-LTE forward and inverse models, and presents the retrieval scheme applied to our dataset. Section 4 shows the results obtained for the CO<sub>2</sub> density. In Section 5 we analyze the sensitivity of the retrieval to the use of a different *a priori* and to several uncertainty sources. Section 6 shows the results for temperature. Section 7 presents a short discussion on the comparison of the results to simulations and other instruments. Finally Section 8 summarizes this work, giving possible improvements, and suggests future applications to the retrieval scheme.

## 2. The OMEGA limb observations at 4.3 μm

The OMEGA instrument is an imaging spectrometer with three spectral channels covering the 0.35 to 5.1 μm spectral range, with a variable spectral resolution. A full description of the instrument and its ground calibration can be found in Bibring et al. (2004). The CO<sub>2</sub> 4.3 μm emission falls within the range of the long-wavelength IR (LWIR) channel, which covers from 2.6 to 5.1 μm with a resolution of 20 nm. This channel consists of a 200 mm Cassegrain telescope with a fore-optics to provide cross-track scanning, a beam splitter (all elements shared with the short-wavelength IR (SWIR) channel), and an actively cooled detector array (Bibring et al., 2004). While the spectral resolution is not high, the main advantage of OMEGA is its fine spatial sampling, which translates in an altitude resolution of around 1 to 9 km when looking at the limb from the Mars Express orbit.

While most of the time OMEGA works in nadir mode to achieve its main scientific goal, mineralogical characterization of the Martian surface, some atmospheric observations using limb geometry are also performed. The first analysis of OMEGA atmospheric limb observations of 4.3 μm non-LTE emissions was presented by Piccialli et al. (2016), but they did not perform retrievals. Further details about the instrument, the treatment and corrections applied to the LWIR channel and the data acquisition are found there. We made use of these corrections in this work, as detailed below.

### 2.1. The dataset, calibration and cleaning

A total of around one hundred OMEGA limb dayside *qubes*, covering from 2004 to 2010 (Martian Years 26–30), are available and will be the final target of our study. From this dataset we selected three representative orbits to illustrate the behavior of our retrieval scheme. Table 1 lists the geolocation and number of vertical profiles generated for each of the three selected data *qubes*.

OMEGA data are presented in *qubes*, 3-D datasets with the two spatial dimensions of the field of view plus the spectral dimension. We started the OMEGA data analysis using the *qubes* level 0 (non-calibrated) observations publicly available at the ESA Planetary Science Archive (PSA, 2019). Fig. 1 shows the distribution of the available spectral data according to their altitude, longitude, latitude and solar zenith angle, for the case of the 0330\_2 data *qube*, corresponding to observations on 2004/23/04.

For each of the three orbits we performed the following calibration and preprocessing steps:

- First we needed to change the calibration pipeline provided by the OMEGA team, because a cut-off at a constant radiance was applied to the observed radiances at all tangent heights. Fig. 2 (left panel) shows this apparently arbitrary radiance cut-off at different wavelengths for orbit 0330\_2. As can be seen, all measurement points below a given radiance were assigned a fixed value or minimum radiance. As a consequence, an accumulation of data appears in that minimum radiance where the signal is strong, and this is why it was unnoticed so far. However it would cause an undesired and very critical effect on limb observations at high altitudes, where the signal is close to zero.
- Then we performed a geometric correction for the altitude registration of the LWIR channel, as described in Eq. (1) of Piccialli et al. (2016). This correction introduced a vertical shift with an orbit-dependent sign. To decide the sign of the shift, we compared the corrected spectra with the prediction of our forward model, calculated for the atmospheric conditions extracted from the GCM at the time and the location of the observed orbit (Fig. 2, right panel). We also used the empirical modification as described by Jouget et al. (2009) to correct for radiance variations in the calibration level with respect to its nominal value before launch. For more details, see Audouard et al. (2014).
- Then we corrected in wavelength, with a shift of +1, 0 or -1 spectel, i.e., one spectral grid point, by inspecting all spectra shapes between 4.2 and 4.4 μm, because there is a known shift of this magnitude affecting most of the spectra (Piccialli et al., 2016). This was done by adjusting the spectral position of the well-known contribution of several narrow CO<sub>2</sub> bands around 4.3 μm (López-Valverde and López-Puertas, 1994a).
- Finally we analyzed the spectra using a clustering algorithm, k-means (with k, the number of clusters, equal to 15 (MacQueen, 1967)). This unsupervised algorithm groups similar data together, helping to find underlying patterns. Thus, it makes the detection of singular spectra (spurious, instrumentally affected or influenced by a local perturbation) easier. The application of this clustering algorithm to the OMEGA *qube* gave k groups in which the spectral

**Table 1**

Geolocation of the limb observations center and profile information for the three orbits analyzed.  $\Delta\text{Lat}$  is the latitude step between adjacent profiles within a *cube*. Columns for latitude (Lat), longitude (Lon), solar zenith angle (SZA), solar longitude ( $L_S$ ) and latitude step ( $\Delta\text{Lat}$ ) are all in degrees. The units for local time (LT) are hours. # profiles is the number of vertical radiance profiles built for each *cube*. The last column shows the percentage of convergence obtained for the application of the retrieval to these profiles. The profile information is later used for inversions.

Orbit	Lat	Lon	LT	SZA	$L_S$	# profiles	$\Delta\text{Lat}$	# converged
0044_1	+14.8	79.3	13.7	34.0	338	11	0.02	11 (100%)
0330_2	+19.5	47.0	12.9	14.5	23	24	0.10	24 (100%)
0647_1	+59.0	310.0	7.5	54.0	64	12	0.09	7 (58%)

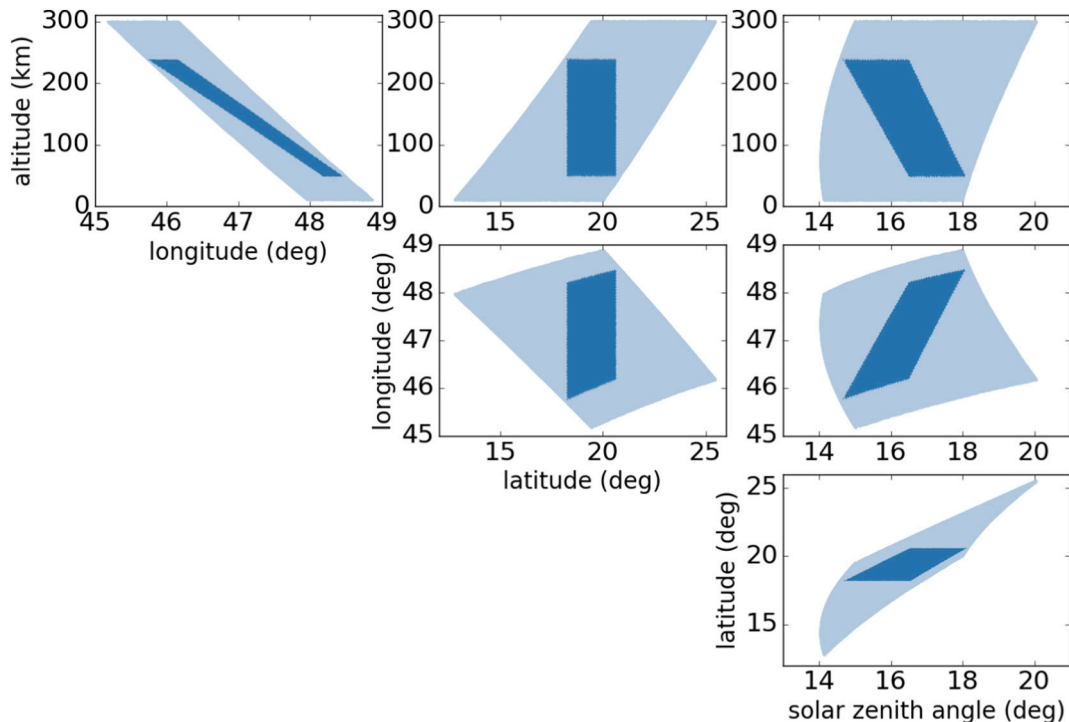


**Fig. 1.** Projection on the limb of the location of spectral data for the OMEGA orbit 0330\_2, in different 2-D planes: LON-ALT, LAT-ALT, SZA-ALT, LAT-LON, SZA-LON and SZA-LAT. Each individual point (not resolvable in the figures) corresponds to a complete spectrum, totaling 20,801 spectra. The observations actually used for the generation of the radiance vertical profiles are highlighted in dark blue. See text for details. (For interpretation of the references to color in this figure legend, the reader is referred to the web version of this article.)

observations were distributed. Each group could be characterized by representative spectra. Non-physical spectral shapes (far from the expected spectral shape at the given tangent height, according to the non-LTE model) were eliminated. Fig. 3 shows the representative spectra (left panel) and the distribution of the data into the 15 groups (right panel). A fundamental result of this clustering analysis is that the spectral shape variations in a typical *cube* are due to the altitude, not to the horizontal coordinates latitude and longitude, which is exploited for the vertical binning (see below).

No groups (spectra) were rejected in the orbit used as an example. However, the use of this technique was useful for other observations (only a small fraction were rejected). As an example, Fig. 4 shows the representative spectra (left panel) and the distribution of the data into the 15 groups (right panel) for orbit 6586\_0. For this *cube*, some observations (like those in group 14) presented an incorrect behavior, probably due to an instrumental artifact, and were removed for that reason.

## 2.2. Generation of radiance vertical profiles

Once the data were calibrated and cleaned, the radiance vertical profiles were built by performing a vertical and latitudinal binning,

forming an altitude-latitude grid, and then combining the spectra available for each box. The generation of the radiance vertical profiles for dataset 0330\_2 is presented in this section as an example.

As shown in Fig. 1, for a given orbit, the coverage in the two horizontal variables latitude and longitude are linked. Therefore only one of these is needed for averages of spatially close observations. These averages are necessary to avoid large spectral variations in the horizontal dimension, and we made these averages in latitude, with a bin size of  $\Delta\text{Lat} = 0.1$  deg, and in altitude, with a uniform spacing of 2 km in tangent height. This, together with the small variation in solar zenith angle (typically smaller than 8–10 deg), guaranteed homogeneous non-LTE conditions (López-Puertas and Taylor, 2001; López-Valverde et al., 2011, 2016). On average, between 12 and 30 profiles per data *cube* were produced, all extending from 50 km to about 200–250 km. The actual number depended on the 2-D limb projection of the dataset. Fig. 5 (left panel) shows the location of the 24 profiles generated for orbit 0330\_2, separated by 0.1 deg in latitude. Each profile consists on a series of boxes 2 km wide in the vertical and 0.1 deg in latitude, where the available observations are combined together.

For every vertical profile, an evaluation of a systematic bias and a random component was performed. Both were estimated by combining all the data above 250 km, where the radiance is expected to be close to zero (below the measurement noise) on average. The first component,

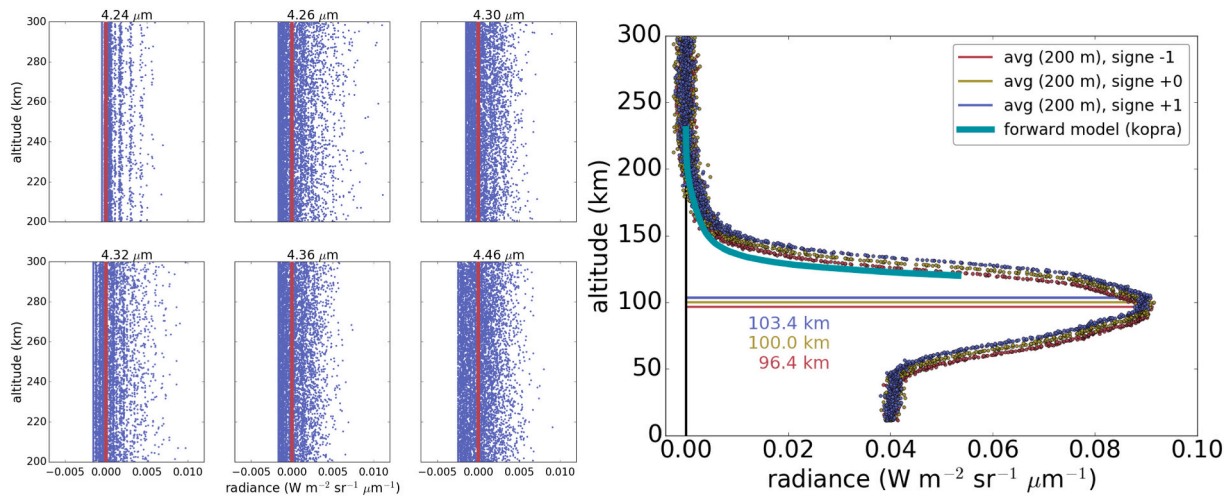


**Fig. 2.** *Left:* Radiance vertical profiles of orbit 0330\_2 between 200 and 300 km. The red lines represent the zero radiance level. *Right:* Radiance vertical profiles of orbit 0330\_2 after applying the LWIR shift correction with different signs, compared with the forward model prediction for atmospheric conditions of the GCM. The vertical profiles are averaged using a bin of 200 m. The numbers in the plot refer to the altitude of the peak. For orbit 0330\_2, the sign selected for the shift correction is  $-1$  (see Piccialli et al., 2016), as it gives a closer value to the forward model calculation (thick solid blue line). (For interpretation of the references to color in this figure legend, the reader is referred to the web version of this article.)

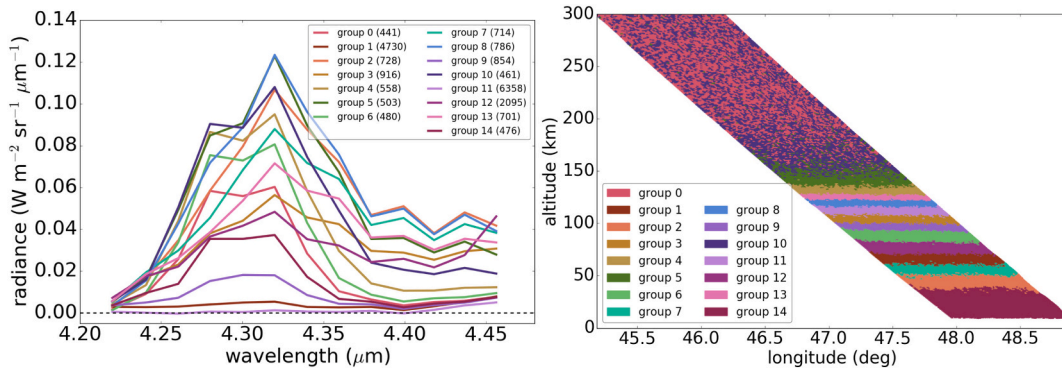


**Fig. 3.** *Left:* Spectra for cluster centers (clustering parameter  $k = 15$ ) for orbit 0330\_2. Colors correspond to cluster identifiers, and the numbers between parentheses refer to the number of spectra in the group. The spectral shape of the cluster centers allows accepting or discarding groups of spectra easily. The signal beyond 4.45  $\mu\text{m}$  is due to the contribution of lower altitudes. At the altitudes of interest for the present study, i.e., above 120 km, the signal is negligible at wavelengths shorter than 4.35  $\mu\text{m}$ . *Right:* Distribution of the spectra into different groups after clustering. Colors correspond to cluster numbers. The grouping mainly follows a distribution as function of tangent height, as expected for non-LTE radiation. See text for details.

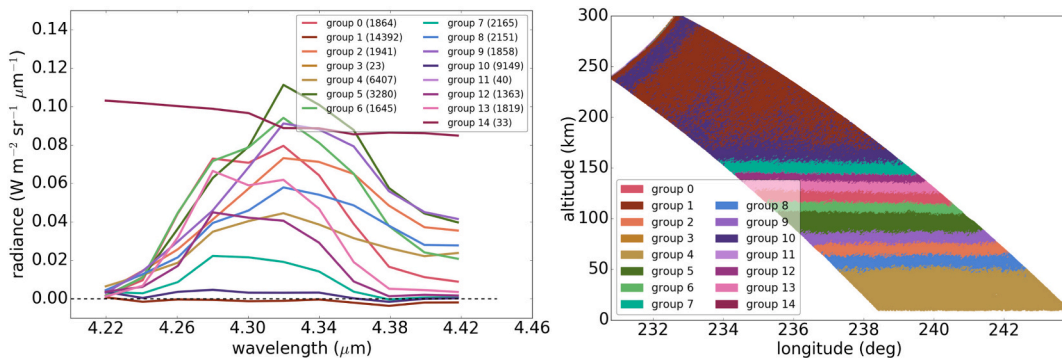


**Fig. 4.** Same as Fig. 3, for orbit 6586\_0. The spectral shape corresponding to the cluster center of group 14 (left panel) is clearly incorrect, hence the 33 observational points in group 14 were discarded. A small number of spectra, 23 and 40, fall in groups 3 and 11 respectively, which are not displayed on the left panel as they lay outside the scale chosen here; these were also discarded. The three discarded groups occur at the very top altitudes, in the last rows of the cube, and are hardly visible in the right hand side panel given their small size.

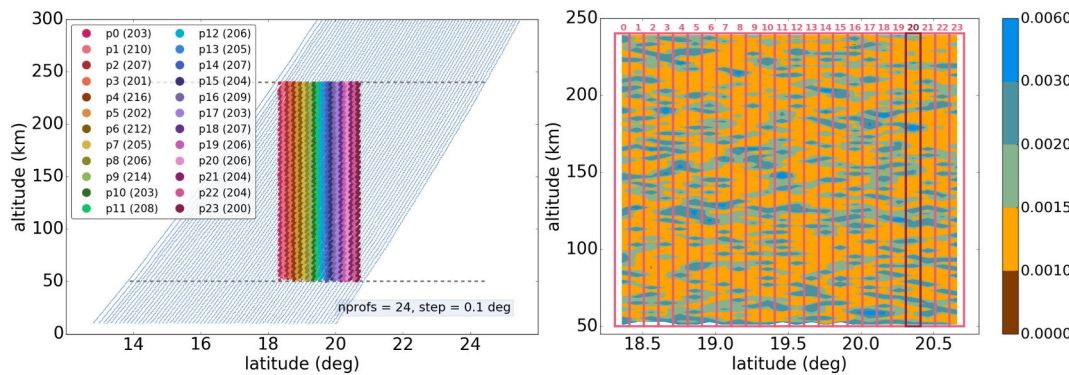


**Fig. 5.** *Left:* Geolocation of the 24 vertical profiles for orbit 0330\_2. Different colors correspond to individual vertical profiles, and the number in parentheses accounts for the total spectra belonging to each profile. The pale blue dots in the background correspond to the geolocation of the OMEGA observations, like in Fig. 1. *Right:* Calculated measurement error ( $\text{W m}^{-2}\text{sr}^{-1}\mu\text{m}^{-1}$ ) for the 24 vertical profiles, at 4.30  $\mu\text{m}$ , which can be compared to typical noise and offset values in Fig. 2 above. Profile #20 is highlighted in dark red. See text for details. (For interpretation of the references to color in this figure legend, the reader is referred to the web version of this article.)

the deep space radiance offset, was computed from the mean of the radiances measured above that tangent height, and was used to correct for the signal bias at all altitudes. Typical space offsets in the 4.3  $\mu\text{m}$  region were presented by Piccialli et al. (2016), and vary between 0.004 and 0.006  $\text{W m}^{-2}\text{sr}^{-1}\mu\text{m}^{-1}$ . This is about similar to the random component in the altitude–latitude boxes in Fig. 5 (right panel) and about 1/20 times the peak emission in the center of the band in Fig. 3 (left panel). The second one, the noise equivalent spectral radiance or  $\text{noise}_{\text{TOA}}$ , was calculated from the standard deviation of these radiances and was later used to obtain the noise for every box.

Fig. 5 (right panel) shows the measurement noise for every profile in orbit 0330\_2, on an altitude–latitude projection. The measurement noise for each box was estimated by computing two different values:

- the standard error of the mean for the spectra in the box, and
- the measurement noise at the top of the atmosphere,  $\text{noise}_{\text{TOA}}$ , divided by the square root of the number of spectra in the box.

When the number of points in the boxes is large, and there are not systematics, these two terms should coincide because they are estimates of the same magnitude, and we confirmed that this is the case. Regardless of the number of points in each box, in this work we selected the maximum of the two terms as a conservative approach. If a box contains only one spectrum, the maximum of the noise value of the neighbor boxes was used.

Fig. 6 shows the averaged radiance vertical profiles (left panel) and the averaged spectra at different tangent heights (right panel), with the

noise values computed for every binned spectrum, for profile #20 of the OMEGA orbit 0330\_2, after correcting the radiances for the deep space offset (calculated above 250 km). These are the data to be supplied to the inversion scheme (see next section). These results are similar to those in Fig. 1 of Piccialli et al. (2016). They confirm the same gross features, like the increase of the limb non-LTE emission with tangent altitude up to a peak in the mesosphere and a strong decrease above. Piccialli et al. (2016) did not bin the data in altitude.

### 3. The Mars non-LTE inversion scheme

The Earth's forward model adopted for the present study combines a generic non-LTE radiative transfer algorithm, the *Generic RAdiative traNsfer AnD non-LTE population Algorithm* (GRANADA) (Funke et al., 2012), with a well tested line-by-line radiative transfer model, the *Karlsruhe Optimized and Precise Radiative transfer Algorithm* (KOPRA) (Stiller, 2002). GRANADA computes the CO<sub>2</sub> non-LTE populations of a large set of vibrational states for a given atmospheric state, which are used by KOPRA for the calculation of the infrared radiances emitted by the assumed atmosphere in the requested (limb) geometry.

The flexibility of GRANADA allowed for an easy adaptation of the terrestrial CO<sub>2</sub> non-LTE scheme to the Martian atmosphere. GRANADA CO<sub>2</sub> non-LTE populations were compared to those calculated with another non-LTE model for CO<sub>2</sub> atmospheres also developed in our group (López-Valverde and López-Puertas, 1994a; Roldán et al., 2000; López-Valverde et al., 2016), and good agreement was found (not shown). Small differences in some state populations could be attributed

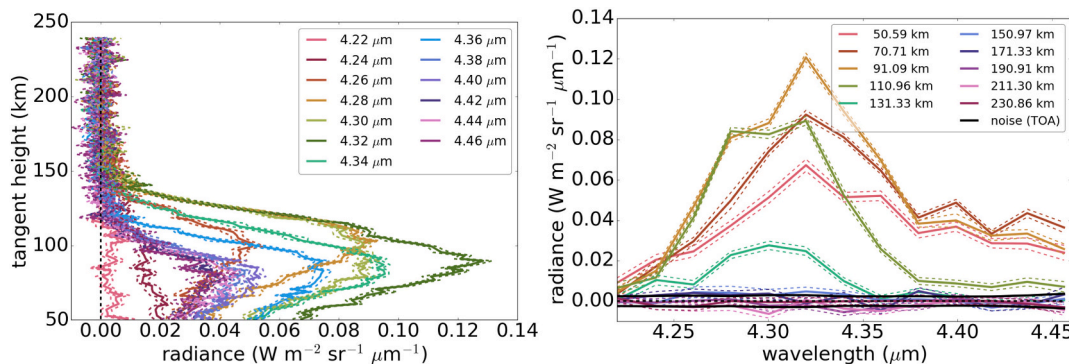


**Fig. 6.** *Left:* Spectral radiances at different wavelengths for profile #20 of the OMEGA orbit 0330\_2, after correcting for the spatial offset. The dashed lines represent the measurement noise. The spectra correspond to latitudes between 20.31 and 20.41 deg. Different colors are used for different wavelengths. *Right:* Spectra with measurement noise (dashed) for the same profile. Colors correspond to different tangent heights. (For interpretation of the references to color in this figure legend, the reader is referred to the web version of this article.)

to the different radiative transfer and set of vibrational states included. A detailed manuscript describing and comparing both models is under preparation.

The main characteristics of our inversion scheme are summarized in Jurado-Navarro (2015), where the retrieval of CO<sub>2</sub> abundance from MIPAS spectra in the Earth's upper atmosphere was successfully tackled.

From the description of the inverse problem in remote sensing (Rodgers, 2000; von Clarman et al., 2003a, 2003b; von Clarman et al., 2019), a solution is typically achieved by an iteration process written as

$$\vec{x}_{i+1} = \vec{x}_i + [\mathbf{K}^T \mathbf{S}_y^{-1} \mathbf{K}]^{-1} \times [\mathbf{K}^T \mathbf{S}_y^{-1} (\vec{y} - \mathbf{F}(\vec{x}))], \quad (1)$$

where  $\vec{y}$  is a vector of measurements (in our case, a set of observed limb spectra at certain altitudes, in a given spectral range and resolution), with dimension  $M$  (number of tangent heights where observations are available),  $\vec{x}$  is a vector of retrieval parameters, in our case CO<sub>2</sub> density between 50 and 200 km, binned every 2 km, with dimension  $N$  (number of tangent heights where CO<sub>2</sub> is inverted),  $\mathbf{F}(\vec{x})$  is the non-linear function representing the formal solution of the radiative transfer equation,  $\mathbf{K}$  is the Jacobian, a matrix of  $M \times N$  dimensions (in which each element is the partial derivative of a forward model element with respect to a state vector element), and  $\mathbf{S}_y$  is the measurement covariance matrix. This is a diagonal matrix, build from the measurement noise, because we have not observed any clear spectral correlation in this noise.

The forward model,  $\mathbf{F}(\vec{x})$ , is an essential piece of every inversion process. In our case,  $\mathbf{F}$  consisted on a precise line-by-line radiative transfer calculation with a careful handling of geometrical conditions, ray-tracing, angle integration, instrumental line shape, etc. Under non-LTE conditions, the forward model additionally requires the calculation of the energy state populations of the species responsible for the emissions, which is CO<sub>2</sub> in our case. This was performed with the GRANADA non-LTE model, developed for the species at work (CO<sub>2</sub>) and adapted to Mars in this work.

For a reasonable solution of the state vector, some *a priori* information,  $\vec{x}_a$ , is frequently required. The inverse problem is usually an ill-posed problem, and its solution is very sensitive to noise propagation. We therefore included a smoothing constraint by means of a 1st-order Tikhonov regularization matrix,  $\mathbf{R}$ , which ensured independence on the *a priori* absolute values. Notice that this is different to the very

common “optimal estimator” approach, which uses the inverse of the covariance matrix of the *a priori* for the regularization (see von Clarman et al. (2019) for an in-depth discussion). The matrix values were chosen as a trade-off between an acceptable vertical resolution and a reasonable retrieval noise error (as the regularization increases, the degrees of freedom, and hence the vertical resolution, decrease, and the retrieval noise error decreases). More details can be found in von Clarman et al. (2003a, 2003b).

Finally, to avoid problems with strong non-linearities during the iteration process, we used a Levenberg-Marquardt (LM) damping (Levenberg, 1944; Marquardt, 1963), following the same method described in von Clarman et al. (2003a, 2003b).

Considering all these terms, the solution to our inverse method is given by

$$\vec{x}_{i+1} = \vec{x}_i + [\mathbf{K}^T \mathbf{S}_y^{-1} \mathbf{K} + \mathbf{R} + \lambda \mathbf{I}]^{-1} \times [\mathbf{K}^T \mathbf{S}_y^{-1} (\vec{y} - \mathbf{F}(\vec{x})) - \mathbf{R}(\vec{x}_i - \vec{x}_a)], \quad (2)$$

where  $\lambda$  is the Levenberg-Marquardt damping factor, forced to be zero in the last iteration.

Eq. (2) was iteratively solved starting from an initial guess and using spectra and Jacobians calculated by KOPRA, and non-LTE populations provided by GRANADA (see Fig. 7). The measurement covariance matrix was calculated from the noise-equivalent spectral radiance of the measurements. Convergence was reached when the change of the retrieval parameters with respect to the previous iteration was smaller than a given fraction of the retrieval noise error (60%). The main outputs were the retrieved parameters (CO<sub>2</sub> density) in addition to diagnostics, such as the averaging kernels, the noise error covariance matrix or the vertical resolution.

Our retrieval scheme is shown in the sketch of Fig. 7 and followed five steps:

- the *a priori* information on the CO<sub>2</sub> density was introduced in KOPRA and GRANADA;
- GRANADA calculated the CO<sub>2</sub> non-LTE populations;
- KOPRA used the non-LTE populations to compute the outgoing (emerging from the atmosphere) radiances and the Jacobians, i.e.,

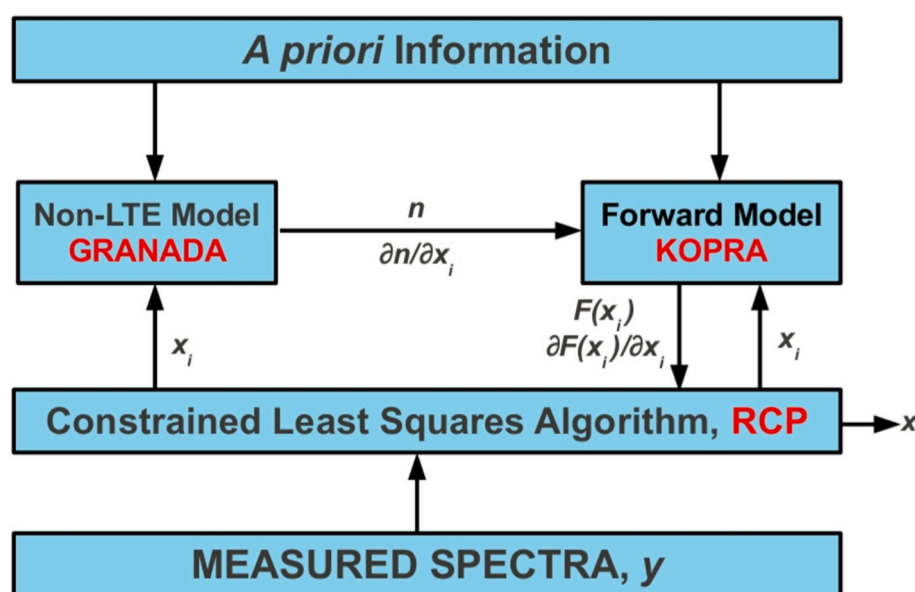


**Fig. 7.** The IMK-IAA non-LTE retrieval scheme, adapted from Jurado-Navarro (2015).  $x_i$  is the vector of the retrieval parameters at each iteration step,  $x$  is the output vector of retrieval parameter, and  $n$  are the non-LTE populations from GRANADA. KOPRA calculates the simulated spectra,  $F(x_i)$ , and the Jacobians,  $\partial F(x_i) / \partial x_i$  at each iteration.

- the derivatives of the radiances with respect to the retrieval parameters;
- the simulated spectra and the measured (or synthetic) spectra were passed to the retrieval control program (RCP) for iteration;
  - if the result did not satisfy a convergence criterion, the result was sent back to KOPRA and GRANADA for recalculation, otherwise the retrieved data were obtained. The usual convergence criterion in RCP is that the residuals are within a fraction of the measurement noise.

Retrievals for both synthetic and measured spectra were performed under Martian conditions with OMEGA instrumental characteristics. Below 120 km we found strong non-linearities in a very optically thick regime, where both the non-LTE CO<sub>2</sub> populations as well as the limb radiances strongly depend on the CO<sub>2</sub> density. This led to non-convergence in many cases. For that reason, the CO<sub>2</sub> profile was regularized by means of a Tikhonov-type smoothing with a strong constraint below 100 km, in order to force the retrieved CO<sub>2</sub> to be close to the climatological density (*a priori*) shape in the lower mesosphere. Above 100 km, the constraint was optimized, by modifying the regularization on a trial-and-error approach, to obtain stable calculations with a precision high enough to allow for meaningful retrieved CO<sub>2</sub> abundances above 120 km.

#### 4. Retrieval of CO<sub>2</sub> profiles

##### 4.1. Atmospheres from the GCM

The retrievals were performed for both synthetic (*i.e.*, generated by a forward model) spectra, for test purposes, and real measurements, as observed by OMEGA. For both cases, the reference temperature, pressure and abundance profiles were taken from specific runs of the LMD Mars GCM (González-Galindo et al., 2015), using monthly averages for Martian Year 27 (MY27). The temporal standard deviation (STD) of the model outputs during that period were also extracted and considered as a measure of the reference atmosphere uncertainty; these values were used as a source of uncertainty during the error analysis (sensitivity studies) in Section 5. The extraction of these quantities was done at the closest point of the GCM grid, which is 3.75 deg × 5.625 deg wide, and the model time step is 2 h. Given the size of the limb portion of most OMEGA *qubes* studied here, a single extraction of the *a priori* from the LMD-MGCM, common to all the vertical profiles in the *qube*, is sufficient.

Fig. 8 shows the reference temperature and pressure profiles (left panel) corresponding to orbit 0330\_2 (see Table 1). For illustrative purposes, its right panel shows volume mixing ratio (vmr) profiles of a few species of importance for the non-LTE CO<sub>2</sub> state populations (N<sub>2</sub>, CO, O(<sup>3</sup>P), O<sub>2</sub>) and of H<sub>2</sub>, a key species for the diffusive equilibrium at thermospheric altitudes.

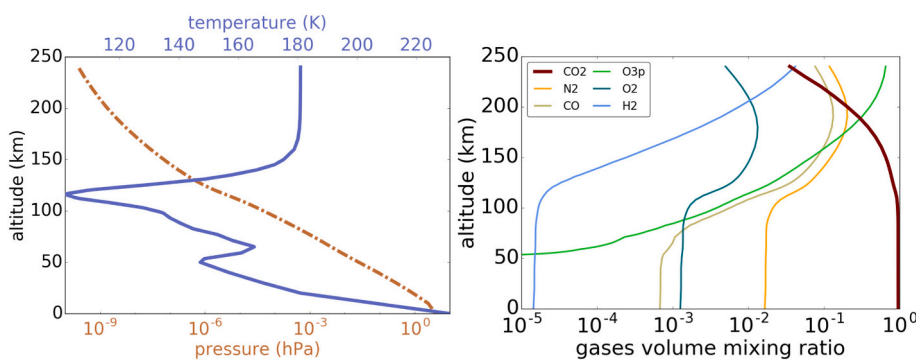


**Fig. 8.** Left: Temperature (solid) and pressure (dash-dotted) of the reference profile, as taken from the Mars GCM for MY27 for the *qube* 0330\_2. Right: *A priori* vmr of CO<sub>2</sub> and abundance of other species included in the GCM.

#### 4.2. CO<sub>2</sub> density retrievals

The data *qube* 0330\_2 was split into 24 vertical profiles, individually processed, with small latitude steps among them ( $\Delta\text{Lat} = 0.1$  deg). Fig. 6 (left) shows the profile #20, that is used as an example of the inversion process throughout this section.

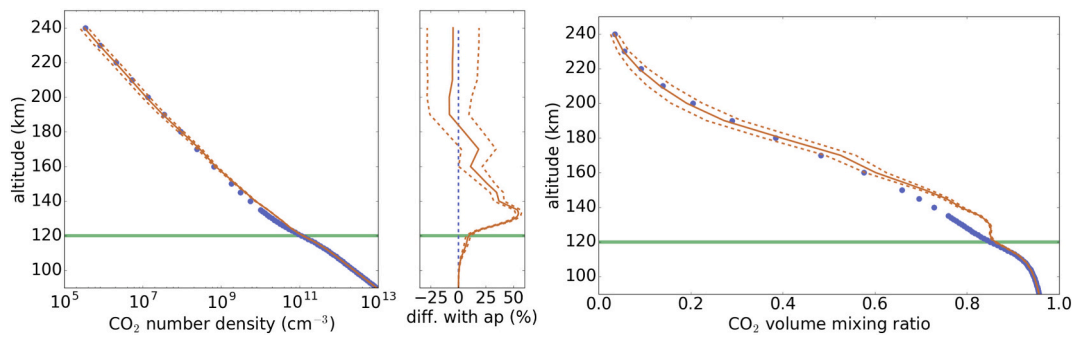
In the retrieval process the convergence was achieved when the difference in the spectra between two consecutive iterations (computed globally by a chi-squared method) was smaller than 0.6 times the measurement noise. For this example, the convergence was reached after 3 iterations. The solution obtained is the best one compatible with observations, as it was reached after a minimization of a chi-square functional. It was also found to be independent on the first guess, and presented robustness against changes in diverse parameters (noise values, *a priori* information and regularization).

Although our retrieval product is the absolute abundance of CO<sub>2</sub>, its relative value (or vmr) is also useful for comparison purposes and to illustrate more clearly any vertical variation. For this purpose, an estimate of the total density was needed, and we computed one by adding to the retrieved CO<sub>2</sub> density the individual densities of the remaining minor constituents, taken from the GCM. This is equivalent to extract the total density from the GCM and correct it with our retrieved CO<sub>2</sub>. Therefore, the vmr shown in Fig. 9 (right panel) is only an estimation made by mixing observations and model results. This method of building a VMR has the virtue of being simple and easily applied or scaled to other datasets.

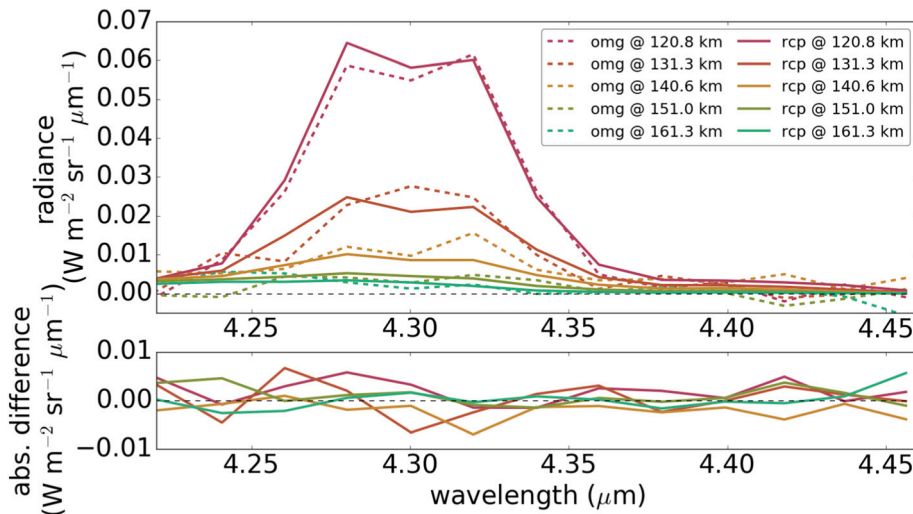
The retrieved density is meaningful only between 120 and 180 km. Below 120 km the retrieval process was strongly regularized, while at the uppermost altitudes the radiances and their inversion are severely affected by noise, as can be seen in Fig. 6. The strong regularization assumed below 120 km is introduced as a strong diagonal constraint to the regularization matrix. This way, the retrieved density is not able to depart from the *a priori* values. Above 180 km, the first-order Tikhonov regularization does not fix the retrieved profile to the *a priori* in absolute terms but the retrieved density mimics the *a priori* shape (vertical gradients).

Fig. 10 shows the spectra obtained at different tangent heights from the last iteration of the retrieval, compared with the measured spectra. In Fig. 11 the derived radiance vertical profiles are compared with the observations at four wavelengths. In the same figure, the output radiance from the first run, that is, our forward model (KOPRA) applied to the reference atmosphere, is also shown.

The best fit spectra in Fig. 10 present a double-peak shape around 4.30 μm. The double-peak tends to disappear above a given altitude, usually around 140–150 km, although in this orbit it is slightly higher. This agrees with what was found by Piccialli et al. (2016), who only performed simulations for the climatological atmosphere, but already showed that the double-peak altitude variations depend on the relative contributions of the fundamental and the second hot bands, which is a



**Fig. 9.** *Left:* Retrieved CO<sub>2</sub> number density for profile #20 of orbit 0330\_2 (orange line, with noise error in dashed lines), compared with the *a priori* profile (blue dots). *Middle:* Relative difference of the retrieved CO<sub>2</sub> number density with respect to the *a priori*. *Right:* Same as *left* panel, with the CO<sub>2</sub> abundance expressed as vmr. The total density was not measured but built by adding, to the CO<sub>2</sub> retrieved abundance, the abundance of the rest of gases in the GCM. *Both:* The green line at 120 km represents the lower boundary of the retrievals. Only results above that line are relevant. (For interpretation of the references to color in this figure legend, the reader is referred to the web version of this article.)



**Fig. 10.** *Top:* Best fit spectra for the profile #20 of the OMEGA orbit 0330\_2 (rcp, solid), compared with observations (omg, dashed), at five selected tangent heights. *Bottom:* Differences between best fit and OMEGA. The measurement noise is not shown because varies with altitude, as shown in Fig. 11, but on average it is about  $0.003 \text{ W m}^{-2} \text{ sr}^{-1} \mu\text{m}^{-1}$ .

function of pressure and the actual thermal structure. This behavior is typical in a CO<sub>2</sub> atmosphere, with a limb emission dominated by the fundamental band at high altitudes, but with large contributions from the weaker second hot bands at lower altitudes, where the fundamental band is optically thick (Piccialli et al., 2016; López-Valverde et al., 2011; Gilli et al., 2009). In this spectral region there are many CO<sub>2</sub> ro-vibrational bands that contribute to the emerging spectrum, and with contributions that change with altitude due to their different optical thickness, a result common in planetary atmospheres (López-Puertas and Taylor, 2001).

Differences found between the best fit and the measurements were occasionally larger than the noise, as expected. From a purely statistical point of view, about 66% of the spectral points are between  $\pm 1\sigma$ . This behavior was observed throughout the whole spectral range, inside and outside the major emission, which occurs between 4.25 and 4.35  $\mu\text{m}$ .

A peculiar difference was obtained at a tangent height of 131 km, where the measured spectra shows only a single maximum, at 4.30  $\mu\text{m}$ . If real, this may indicate a colder atmosphere; the typical double peak of the second hot bands at 4.3  $\mu\text{m}$  could indeed be affected by temperature. In very cold conditions this effect could even merge the peaks into one maximum. However, with the modest spectral resolution of OMEGA this effect is only observed in one spectral point, and is close to noise levels, and thus it is not possible to conclude whether this is actually real.

Fig. 12 shows a selection of columns and rows of the averaging kernels obtained. Averaging kernels are excellent diagnostic tools which permit some insight into the behavior of the inversion process. Both columns and rows are depicted for completeness, to illustrate both the vertical resolution (better shown by the averaging kernels' rows) and the response to changes in the true state vector (better shown by the columns). The selection of rows and columns in Fig. 12 simply aims to illustrate the variation with altitude. When the information content is enough, the full width at half maximum of rows and columns of the averaging kernels approximately coincide, and they provide the actual vertical resolution of the retrieved CO<sub>2</sub>. In our case this is about 15 km between 120 and 160 km. When compared to the vertical sampling for this observation, about 3.37 km, and to the vertical binning used to form the radiance vertical profiles, 2 km, this indicates that a larger averaging of the data (bin sizes larger than 2 km) is possible. In addition, the trace of the averaging kernel matrix gives the number of independent pieces of information, *i.e.*, the degrees of freedom, between four and five for profile #20. At higher altitudes, averaging kernels are wider, as expected, since the non-LTE emission strongly decreases with altitude in the optically thin regime.

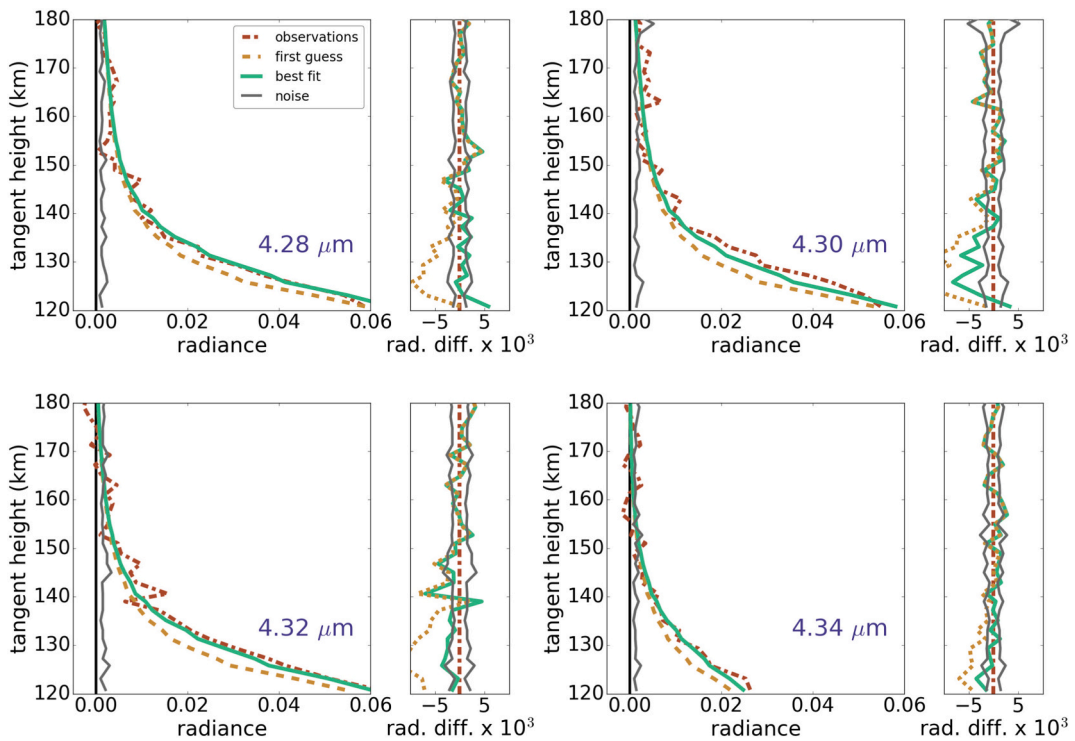


**Fig. 11.** [All panels] Left: Best fit for profile #20 (solid), compared with observations (dash-dotted) and with simulations of the forward model after the first step of the iteration (dashed). Right: Differences with the observations. Measurement noise is added for reference (grey solid lines). All radiance units are in  $\text{W m}^{-2} \text{sr}^{-1} \mu\text{m}^{-1}$ .

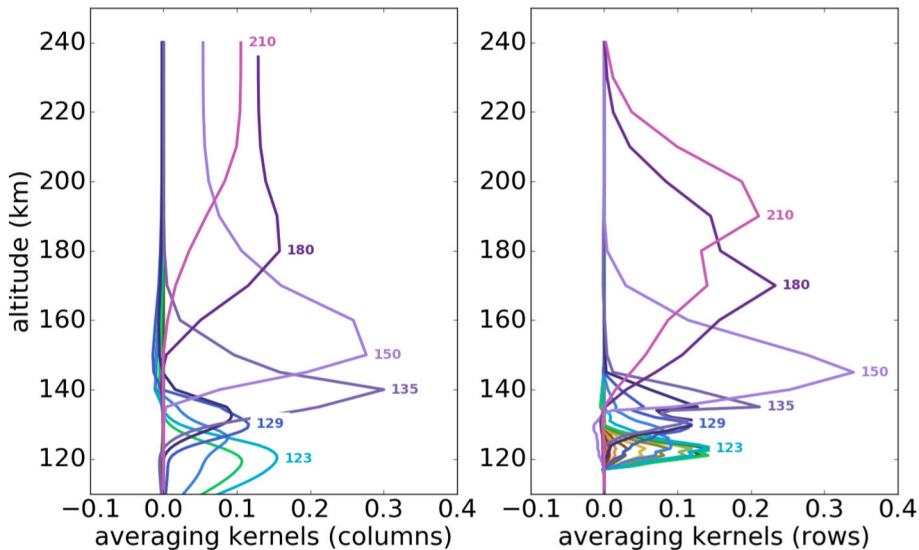


**Fig. 12.** Columns and rows of the averaging kernels resulting from the retrieval process at a selection of 8 tangent altitudes. Different colors represent different averaging kernels and the numbers are the corresponding altitudes in km. For clarity, only one every three columns (or rows) is being represented in the figure. (For interpretation of the references to color in this figure legend, the reader is referred to the web version of this article.)

## 5. Sensitivity and error analysis

### 5.1. Sensitivity to the *a priori* CO<sub>2</sub> abundance

A first estimate of the uncertainty in the *a priori* CO<sub>2</sub> comes from the st.dev. in the GCM outputs, and this gives variations around 10–20%, whose impact on the retrieved densities was very small. To test the retrieval performance against *a priori* CO<sub>2</sub> abundances, we performed a

retrieval with a very different *a priori*, that for orbit 0044\_1 (see Table 1). The new *a priori* abundances are significantly larger than in the nominal case, as can be seen in Fig. 13 (left panel), where the vmr is shown instead of the number density for an easier comparison. The relative differences in these *a priori* profiles is about 50% in the 120–180 km range, but the retrieved CO<sub>2</sub> remained essentially unchanged, except in the uppermost altitudes, but at these altitudes it is within its retrieval uncertainty (right panel).

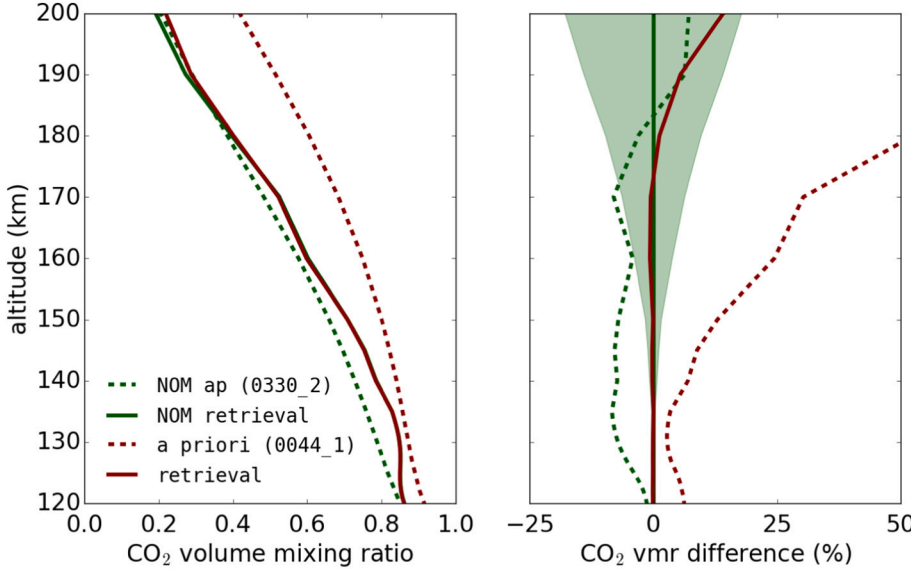


**Fig. 13.** *Left:* *A priori* (dashed red) and retrieved (solid red) CO<sub>2</sub> profiles considering the atmospheric conditions corresponding to orbit 0044\_1, compared to the *a priori* (dashed green) and retrieved (solid green) CO<sub>2</sub> for the nominal case. *Right:* Relative differences with respect to the nominal retrieved CO<sub>2</sub>. The noise error computed for the nominal case is shown as a shaded region. (For interpretation of the references to color in this figure legend, the reader is referred to the web version of this article.)

### 5.2. Sensitivity to parameter uncertainties

A series of sensitivity tests were conducted in order to estimate the impact of the uncertainties in several parameters on the retrieved CO<sub>2</sub> density. The error,  $\epsilon_i$ , associated to the uncertainty of a given parameter,  $\epsilon_p$ , can be described by

$$\epsilon_i = \frac{\partial x}{\partial p} \epsilon_p, \quad (3)$$

where  $x$  is the target variable of the retrieval and  $p$  is the parameter being modified. The partial derivative in Eq. (3) is actually a matrix of dimension  $N \times N$ , where  $N$  is the number of points in the vertical grid. The changes in the parameter,  $\partial p$ , should ideally be introduced at one altitude at a time and the changes in density,  $\partial x$  evaluated at all altitudes. For simplicity and to accelerate the calculation, in this work we made the approximation of introducing perturbations at all altitudes at once. This was tested in several cases against the more rigorous one-altitude-at-a-time study, and found to be a very good approximation, the reason being that all derivatives peaked at the perturbed altitudes.

We present here both random and systematic uncertainties. The most important systematic error sources, *i.e.*, the corrections on pointing and spectral shifts, were addressed during the calibration and preprocessing of the observations (see Section 2). And thus the remaining component of the systematic errors had a stochastic nature. In this work, we considered all the parameter errors,  $\epsilon_i$ , as independent and therefore combined them quadratically, together with the noise error component,  $\epsilon_{noi}$ , to obtain the total error,  $\epsilon_{tot}$ .

$$\epsilon_{tot}^2 = \sum_i \epsilon_i^2 + \epsilon_{noi}^2 \quad (4)$$

**Table 2** summarizes the perturbations in the most relevant parameters that we identified, and the retrieved densities are compared with the nominal inversion, NOM, shown in Figs. 9, 10 and 11. The impact of all sensitivity tests on the total retrieval uncertainty and a global discussion can be found in Table 3 and Section 7, respectively. For clarity, the sensitivity retrievals are grouped in three categories.

#### 5.2.1. Sensitivity to atmospheric parameters

In this first group we focus on perturbations in the atmospheric temperature. This is extracted from the LMD Mars GCM (González-Galindo et al., 2015) for Martian Year 27, as mentioned in Section 4. The GCM temperatures uncertainties have a systematic (model biases) and a

**Table 2**

Summary of the perturbed parameters for the sensitivity tests presented in this work. See text for details.

Test code	Perturbed parameters	Notes
NOM	Nominal	prof#20 (0330_2)
TMP1	GCM temperature profile decreased, 45 K	T <sub>GCM</sub> -45 K
TMP2	GCM temperature profile increased, 45 K	T <sub>GCM</sub> +45 K
SHF1	Radiance shift, $-2.5 \times 10^{-5}$ W	W m <sup>-2</sup> sr <sup>-1</sup> μm <sup>-1</sup>
SHF2	Radiance shift, $+2.5 \times 10^{-5}$ W	W m <sup>-2</sup> sr <sup>-1</sup> μm <sup>-1</sup>
SHF3	Pointing shift, $-1/4 \times$ FoV	-0.84 km
SHF4	Pointing shift, $+1/4 \times$ FoV	+0.84 km
SHF5	Spectral shift, $-1/5$ spectel	-2 cm <sup>-1</sup>
SHF6	Spectral shift, $+1/5$ spectel	+2 cm <sup>-1</sup>
IGN1	Instrumental gain decreased by 10%	Gain ÷ 1.10
IGN2	Instrumental gain increased by 10%	Gain × 1.10
FOV1	Field of view decreased to 1.0 mrad	iFoV <sub>nom</sub> = 1.2 mrad
FOV2	Field of view increased to 1.4 mrad	iFoV <sub>nom</sub> = 1.2 mrad
ILS1	FWHM (ILS) decreased to 12 cm <sup>-1</sup>	FWHM <sub>nom</sub> = 14 cm <sup>-1</sup>
ILS2	FWHM (ILS) increased to 16 cm <sup>-1</sup>	FWHM <sub>nom</sub> = 14 cm <sup>-1</sup>
SFL	Solar flux increased by 1%	s <sub>f</sub> × 1.01
KVV1	Collisional rate halved	k <sub>VV</sub> × 0.50
KVV2	Collisional rate doubled	k <sub>VV</sub> × 2.00

random component related to atmospheric variability. The latter can be estimated from the model's standard deviation. The former is estimated from the deviation of the GCM temperature from the hydrostatically derived temperature using the retrieved CO<sub>2</sub> density profile (see Section 6 below). Here we use the maximum deviation encountered (45 K) in order to provide a conservative uncertainty estimate. Therefore, temperature was decreased and increased in 45 K at all altitudes (tests TMP1 and TMP2, respectively).

#### 5.2.2. Sensitivity to calibration parameters

For these tests, a few parameter errors associated to the data were explored. In tests SHF1 and SHF2 the radiance profile was, respectively, reduced and increased by half of the standard error of the mean at TOA, approximately  $5 \times 10^{-5}$  W m<sup>-2</sup> sr<sup>-1</sup> μm<sup>-1</sup>. This was included at all altitudes, in order to account for possible radiometric calibration biases and for the uncertainty on the space offset. In another tests, all spectra were shifted in altitude to estimate the effects of possible misalignment in pointing (cases SHF3 and SHF4). The shift was chosen to be  $\pm 0.25$  times the field of view expressed in kilometers. This is because we repeated the retrieval with the nominal pointing altitude and with shifts of  $\pm 0.5$  times the field of view, and then chose the inversion giving the best fit.

**Table 3**

Summary of the sensitivity tests and their impact on the total uncertainties of the retrieved CO<sub>2</sub> at tangent heights 120, 140, 160 and 180 km. The percentage of variation is obtained for each sensitivity test by comparing the retrieved densities with those of the nominal case, at the indicated tangent altitudes. The dominant parameters at each altitude are highlighted in blue.

Parameter	Uncertainty	Related tests	@120km	@140km	@160km	@180km
temperature	±45 K	TMP1 and TMP2	-18% 24%	-11% +9%	-24% +27%	-27% +30%
radiometric calibration	±1/2 stderr <sub>TOA</sub>	SHF1 and SHF2	±0.1%	±0.3%	±1.7%	+3.4% -3.2%
pointing	±1/4 FoV	SHF3 and SHF4	+5% -8%	+15% -7%	+18% -0.7%	+20% -1.2%
spectral calibration	±2 cm <sup>-1</sup>	SHF5 and SHF6	-0.8% -0.3%	+0.1% -0.7%	-8% +7%	-15% +16%
instrumental Gain	±10%	IGN1 and IGN2	-16% +20%	-12% +14%	-17% +19%	-16% +19%
field of view	±0.2 mrad	FOV1 and FOV2	±0.6%	+0% +0.2%	-0.1% +0%	±0.1%
instrumental line shape	±2 cm <sup>-1</sup>	ILS1 and ILS2	+1.4% -1.6%	+0.6% -0.7%	±0.3%	+0.7% -0.8%
solar flux	±1%	SFL	±1.7%	±1.2%	±1.8%	±1.8%
collisional rate	÷/× 2.0	KVV1 and KVV2	+1.8% -1.0%	-0.5% +0.3%	-1.0% +0.7%	-0.8% +0.6%
noise error	-	NOM	±1.9%	±3.4%	±10%	±16%
<b>total error</b>	-	-	<b>28%</b>	<b>20%</b>	<b>36%</b>	<b>43%</b>

Regarding the spectral calibration (tests SHF5 and SHF6), we followed the description in Bibring et al. (2004) for the ground calibration goals of the OMEGA instrument, where an accuracy of better than 1/5 of the spectral width was expected, approximately ±2 cm<sup>-1</sup>.

The instrumental Gain was perturbed following Bibring et al. (2004) and Vincendon et al. (2015). Before delivery, the photometric calibration goal was to achieve an accuracy better than 1% spectel-to-spectel (relative) and better than 20% in absolute terms. However, compared to TES (Thermal Emission Spectrometer, on board Mars Global Surveyor), OMEGA showed a Gain accuracy better than 3% in absolute terms when observing in a nadir geometry. Tests IGN1 and IGN2 in Table 2 implement the instrumental Gain uncertainty with a larger conservative variation of ±10%.

Tests were also done by perturbing the spatial and spectral resolutions. For FOV1 and FOV2 we changed the field of view from 1.2 mrad to

1.0 mrad and 1.4 mrad, respectively. These variations follow the suggestions of Bonello et al. (2005) and Bellucci et al. (2006). On the other hand, regarding the instrumental line shape and following Bonello et al. (2005), the FWHM of the ILS was decreased from 14 cm<sup>-1</sup> to 12 cm<sup>-1</sup> in ILS1 and increased to 16 cm<sup>-1</sup> in ILS2.

### 5.2.3. Sensitivity to non-LTE forward model parameters

According to Jurado-Navarro (2015), an uncertainty of 1% in the solar fluxes may be considered conservative around 4.3 μm. Here we assumed a solar flux 1% larger than the nominal one (test SFL). In the last group of perturbations, we introduced variations in some vibrational-vibrational collisional rates of the non-LTE model (part of the forward model). Tests KVV1 and KVV2 included perturbations of a factor 2 in the exchanges of one ν<sub>3</sub> quanta among vibrational states of the same and/or different CO<sub>2</sub> isotopes. This collisional process can be

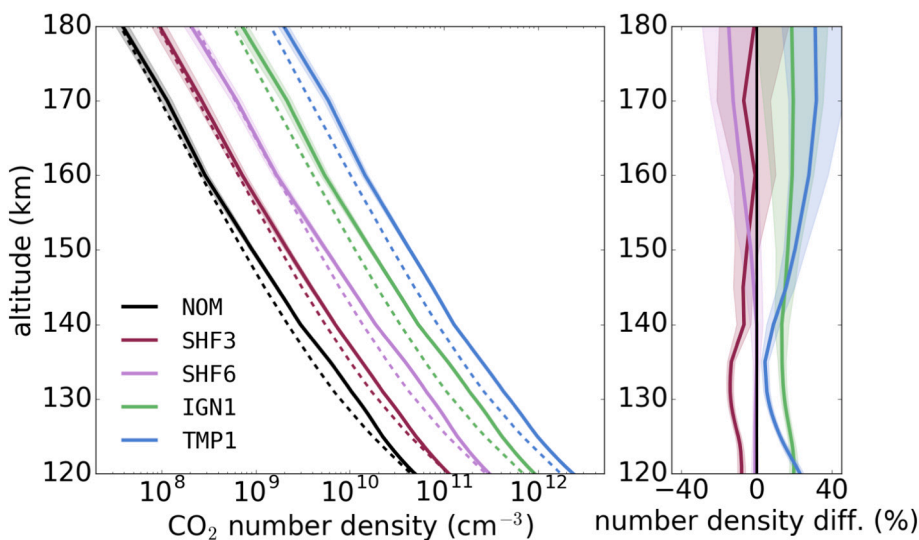


**Fig. 14.** Left: Retrieved CO<sub>2</sub> number density for the nominal case (NOM) and four sensitivity tests (SHF3, SHF6, TMP1 and IGN1), with their *a priori* (dashed) and noise (shaded). Except for SHF3, the profiles are shifted for clarity. Right: Relative differences of the number densities from the sensitivity tests with respect to NOM.

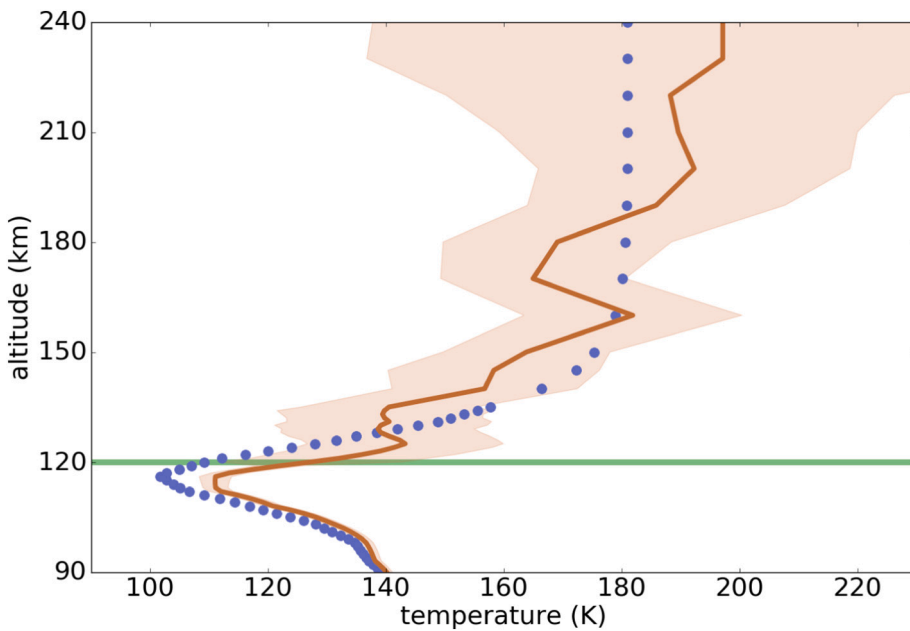
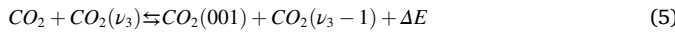


**Fig. 15.** Temperature derived from a hydrostatic adjustment applied to the retrieved CO<sub>2</sub> density (solid orange line). The temperature provided by the GCM is shown with blue dots. The shaded region is the estimated total error (see text for details). The green line at 120 km represents the lower boundary of the retrievals. (For interpretation of the references to color in this figure legend, the reader is referred to the web version of this article.)

described as



Although the number of possible perturbations that can be introduced in the non-LTE model is very large, this V-V collisional exchange was expected to give the largest deviations (López-Valverde and López-Puertas, 1994b). Still the impact on the retrieved CO<sub>2</sub> of these changes in the  $k_{VV}$  was very small. Other collisional processes were also inspected, confirming their negligible contribution to the total error.

### 5.3. Total CO<sub>2</sub> retrieval uncertainties

**Table 3** summarizes the most relevant sensitivity tests performed and their impact in the total uncertainty matrix at 120, 140, 160 and 180 km, while **Fig. 14** shows the retrieved densities for a selection of four perturbations, tests SHF3, SHF6, TMP1 and IGN1. These four were among the most important of the whole set, as pointed in **Table 3**, each one producing a relative variation in the retrieved density up to 20% or larger.

The best fit for the radiance after each of the sensitivity tests was similar to the nominal case, even in these four cases, and are not shown for that reason. No large differences were expected because of the compensation of the CO<sub>2</sub> abundance introduced by the retrieval process. When a larger value of the radiance was needed, the resulting retrieval tended to provide more CO<sub>2</sub> to match the observed spectra, and *vice versa*.

**Table 3** lists both positive and negative errors, although in most cases they are approximately symmetric. The mean of their absolute values was taken in the computation of the total error. As mentioned above, all the perturbations in the table were considered to be independent to each other, and thus they were quadratically combined to obtain the total values. One particular entry in this table is the measurement noise, whose impact on the CO<sub>2</sub> uncertainty is directly computed during the retrieval process.

In the lower thermosphere, below 150 km, the most relevant uncertainties on CO<sub>2</sub> arise from the instrumental Gain and the unknown thermal structure, with moderate values, around 20% for the worst case. The pointing uncertainty is also significant in this region. Since CO<sub>2</sub>

presents a strong emission at these altitudes, the measurement noise has a minor impact. At higher tangent heights, above 150 km, this measurement error becomes as important as the instrumental Gain and the thermal structure. In the upper thermosphere, the spectral calibration and, to a small extent, the pointing have also a significant impact.

### 6. Derivation of temperature profiles

Although the primary goal of this work is to derive CO<sub>2</sub> densities from the OMEGA non-LTE spectra, atmospheric temperature profiles can be derived from the CO<sub>2</sub> retrieved profile with the hydrostatic approximation. This approach has been used in the past in similar situations (Mahieux et al., 2012; Gröller et al., 2015; Thiemann et al., 2018). We implemented an algorithm based on the expression of Theon and Nordberg (1965):

$$T_i = \frac{\int_{z_0}^{z_i} \rho g dz}{\rho_{iM}^R} + \frac{\rho_0}{\rho_i} T_0 \quad (6)$$

In Eq. (6),  $T$  is the temperature,  $\rho$  the CO<sub>2</sub> mass density,  $R$  the gas constant,  $M$  the CO<sub>2</sub> molar mass,  $g$  the gravity,  $z$  the altitude (the variable of integration), and sub-indices  $0$  and  $i$  correspond to the TOA (top of the atmosphere) and layer  $i$  (at altitude  $z_i$ , when the integral is discretised), respectively. We applied this equation to the whole atmosphere, including the homosphere and the diffusive equilibrium region (above about 125 km). Below the homopause, the hydrostatic equilibrium can only be applied to the atmosphere as a whole. However, on Mars, CO<sub>2</sub> is the dominant species and our tests indicate that the error resulting from this approximation in this region was smaller than 5%. We also tested that in the transition region the application of the same equation did not introduce biases, nor changes in the region above.

We applied the algorithm individually to each CO<sub>2</sub> profile. The derived temperature, from the retrieved CO<sub>2</sub> density in **Fig. 9**, is shown in **Fig. 15**, together with an uncertainty bracket, as a shaded region. This uncertainty represents the propagation of the CO<sub>2</sub> retrieval uncertainty through our hydrostatic equilibrium model, and was computed by the quadratic sum of two different noise components: (i) First, a purely random contribution, following a Monte Carlo approach, was calculated by generating 200 density profiles from the mean CO<sub>2</sub> density, by adding

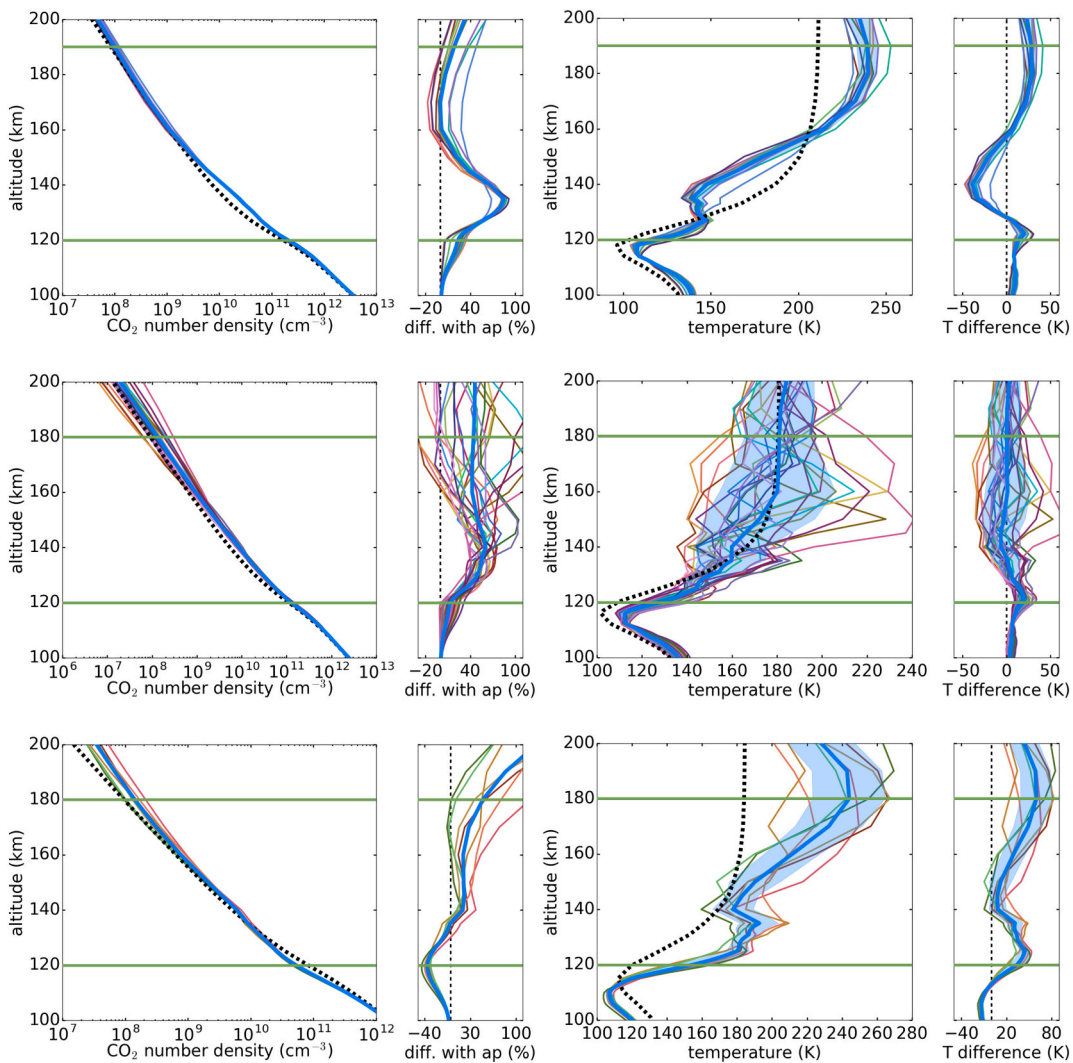


**Fig. 16.** Left: CO<sub>2</sub> number density retrieved for all the profiles in the orbit 0044\_1 (top), 0330\_2 (middle) and 0647\_1 (bottom), each of them with a different color (solid). Their relative differences with the *a priori* density (dashed) are also shown. The average number density for all the profiles in each orbit is represented by a thick blue line. Right: Same for derived temperatures. All: The retrieved quantities contain measurements information only in the region between the solid green lines. (For interpretation of the references to color in this figure legend, the reader is referred to the web version of this article.)

random variations, within the retrieval error of the CO<sub>2</sub> densities at each altitude. For simplicity, we chose density fluctuations of 20%, which is a representative value of the CO<sub>2</sub> noise error, as shown above in Section 5. Then the temperature profiles were obtained and their dispersion computed. (ii) Secondly, computing a systematic contribution of unknown sign due to the downwards propagation of a ±40 K uncertainty on the temperature at TOA. A value of 40 K is about a factor 2 larger than the St.Dev from the GCM for latitude-longitude boxes of 15°, and was chosen in order to reproduce with confidence the model uncertainties in the uppermost thermosphere. This second component was significant only above 140 km, approximately. The temperature uncertainties obtained are typically 20 K in the altitude range of the CO<sub>2</sub> inversion, 120–180 km, and we believe similar values can be considered as representative of the whole OMEGA data set.

Following the same steps described above, we retrieved the CO<sub>2</sub> number density for all the profiles of the three orbits presented in Table 1, totaling 47 individual profiles. We also derived the associated temperature profiles under the hydrostatic assumption. The results are shown in Fig. 16. For all the portrayed profiles, the region between solid green lines corresponds to the altitude range where the retrieved magnitudes contain information on the measurements, from 120 km to the

upper limit imposed by the noise level, which depends on the data *cube* and varies between 180 and 190 km. The averages of both the CO<sub>2</sub> number densities and the temperatures derived for all the profiles in each orbit are shown as solid blue lines.

Fig. 16 shows two important results of the derived temperatures. The first one is that the dispersion in the thermal structure can sometimes be significantly larger than the uncertainty of 20 K discussed above. In the case of orbits 0044\_1 and 0647\_1 it is smaller, but in the case of orbit 0330\_2 (middle panels), the dispersion seems to be larger. The second result is that the averaged thermal structure can be quite different to the model's temperatures. This is the case of orbits 0044\_1 and 0647\_1, with deviations of up to 45 K, more than twice the uncertainty deduced from the CO<sub>2</sub>-profile uncertainties. This largest value was used in the CO<sub>2</sub> error analysis in the previous section.

A brief remark on the variation of the temperature dispersion with altitude may be necessary. Fig. 16 shows that for orbits 0044\_1 and 0647\_1 the dispersion in temperature is small (smaller than the uncertainty from hydrostatics) and slightly increases with altitude. For orbit 0330\_2, however, it increases with altitude but only from 120 to about 160 km, and then decreases at higher altitudes. This is a peculiarity of this orbit and is due to the particular T<sub>0</sub> (temperature at TOA) chosen for

the individual profiles.  $T_0$  is calculated from the CO<sub>2</sub> density gradient at the topmost 2 altitudes for each profile, and the values of  $T_0$  tend to be similar for all the profiles in a given orbit, although it depends on the variability of each case. It turns out that orbit 0330\_2 is particularly homogeneous, with a dispersion of only 2 K, while the other two orbits present variations in  $T_0$  around 20 K.

## 7. Discussion and conclusions

### 7.1. Retrieval performance and limitations

The inspection of Figs. 6 and 9 provides an interesting result. Below a CO<sub>2</sub> density value of about  $3 \times 10^8 \text{ cm}^{-3}$ , or above 180 km in orbit 0330, the atmospheric emission is similar to or smaller than the OMEGA noise level. The measurement noise is an important contribution to the error analysis, as can be seen in Table 3. This density limit was confirmed for the three orbits analyzed in this study, and allowed us to determine a reliability zone, between about 120 and 180 km, shown in Fig. 16 between solid green lines.

Some caution is required when analyzing some of the features obtained in the CO<sub>2</sub> density and in the temperature profiles. Starting with the retrieved CO<sub>2</sub> densities, as shown in Fig. 16 for the three orbits, they are not very different to the *a priori*, although an excess of CO<sub>2</sub> is generally obtained in the lower thermosphere, around 130–150 km. This feature's magnitude is close to the CO<sub>2</sub> density uncertainty and therefore it has to be taken with caution. If real, the larger gradient, compared to the *a priori*, seen in the retrieved densities above 130 km for most of the profiles, translates into temperatures at 140 km colder than those at 130 km (Fig. 16). For both 0044\_1 and 0647\_1 orbits (top and bottom panels), the temperature around 140 km, is indeed colder (about 10–20 K) than that at 130 km, which in principle points to an internal consistency between density and temperature.

However, our temperatures are particularly noisy, as explained above in Sections 5.2 and 6, and the wavy structure observed in the three profiles in Fig. 16 may partially be an artifact. The uncertainty brackets shown in this figure are smaller than our estimate of the temperature bias in the GCM, deduced from the model-data discrepancies in this figure, and are already incorporated into the CO<sub>2</sub> error budget in Section 5.2. Notice also in Fig. 16 that the mean temperatures of the three *qubes* present a positive bias (with respect to the reference atmosphere) around 120 km. This is the very bottom of the retrieval lower boundary, and should also be looked upon with caution; in this case, this is surely an artifact of the strong regularization applied there, *i.e.*, produced by a forced gradient in the CO<sub>2</sub> densities. These densities are larger than the climatology around 130 km, and therefore, present a tendency to the climatological value at the bottom of the inversion range, 120 km, which produces an artificial density gradient (and a too large temperature).

### 7.2. Comparison with simulations and other instruments

Although we only obtained and analyzed here three CO<sub>2</sub> density profiles, we performed a few comparisons of the retrieved densities and the derived temperatures with predictions from the GCM and with observations taken by other instruments. Here we mention some of the main features observed in the comparisons. From the observational point of view, the three orbits studied in the present work (0044\_1, 0330\_2, 0647\_1) do not exhibit special characteristics, and hence the results and retrieval performance presented here may be representative of the entire set of 47 OMEGA *qubes* with useful limb observations. The application of the present inversion scheme to the 47 OMEGA orbits, their analysis and a more extended comparison with global models are in preparation.

Starting with the LMD-MGCM (Forget et al., 1999; González-Galindo et al., 2015), this shows an overall good agreement. However, our retrieved CO<sub>2</sub> density is systematically larger than the model above 130 km, by 30–50%. This is above the total uncertainty at these altitudes

(28%–20% in the 120–140 km altitude range; see Table 3). The temperatures obtained above 130 km present a larger dispersion than the model ones, globally speaking. However, this may also be due to our particularly large uncertainties in this parameter. Regarding the standard deviation of the GCM model's outputs, these obviously depend of the size of the 3-D grid boxes defined at the OMEGA observations. For boxes of 15° in latitude, 15° in longitude and of 2 h, the GCM CO<sub>2</sub> VMR shows variations between roughly 10% and 25% in the range 120–180 km. These are smaller than our uncertainties by a factor 2. However, there are indications that GCMs underestimate the observed variability Piccialli et al. (2016). Hence, the precision achieved in this work can be very informative for exploring atmospheric variability in those spatial and time scales, and very useful to validate the GCM densities.

Recent observations in the diurnal thermosphere were performed by instruments on board the MAVEN mission (Jakosky et al., 2015), namely NGIMS, EUVM and IUVS. First, regarding densities, the reported uncertainties from these experiments are of the order of those presented in this work, which are good news from the perspective of comparative studies and mutual validation. Secondly, all measurements at these altitudes reported important differences when compared to the LMD-MGCM or other General Circulation Models (Medvedev and Yiğit, 2012; Medvedev et al., 2015; Evans et al., 2015; Gröller et al., 2015; England et al., 2017; Terada et al., 2017; Gilli et al., 2017; Bouger et al., 2017; Zurek et al., 2017; Thiemann et al., 2018; Gröller et al., 2018). This points to some needs in the validation of the current GCMs at thermospheric altitudes. Possible biases in the model include a poor representation of gravity waves, although the problem is harder than that, since most, if not all, the datasets available nowadays for model validation share an important limitation. They do not cover the lower atmosphere, whose state has to be assumed (based on current climatologies). Let us recall that the “non-sounded lower atmosphere” in many cases includes the whole troposphere and mesosphere, as it is the case of the effective altitudes in these OMEGA retrievals. This is a complication for reaching a convincing framework for mutual validation.

## 8. Summary

We adapted a non-LTE retrieval scheme extensively used for the Earth atmosphere to Martian conditions for the first time. Internal consistency and sensitivity tests confirmed a working scheme to retrieve CO<sub>2</sub> abundance profiles from observations of its daytime emission at 4.3 μm by the OMEGA instrument on board Mars Express, although its application was limited in tangent height to the 120–180 km range. The vertical resolution is about 15 km in this altitude range. In order to derive temperature profiles from the retrieved densities, we developed an algorithm, assuming hydrostatic equilibrium and including a Monte Carlo scheme to compute the error propagation of the density uncertainties.

The CO<sub>2</sub> inversions for three orbits (0044\_1, 0330\_2 and 0647\_1) are presented, as case studies, to demonstrate the performance of the retrieval scheme. The sensitivity and performance of the CO<sub>2</sub> retrieval is similar in the three orbits. The CO<sub>2</sub> densities retrieved in the three cases show a general agreement with the GCM predictions, within the estimated uncertainties, although systematically higher around 130 km. Regarding the temperatures, we did not obtain any clear trend, common to the three orbits. The profiles derived for the three geo-locations were rather different, and when compared with the GCM they show large discrepancies, up to about 45 K. These suggest large systematic uncertainties when using the GCM thermal structure as *a priori* in the CO<sub>2</sub> inversion.

We generated level 1 vertical radiance profiles for about one hundred OMEGA limb observations, a dataset which can be provided by the authors to whoever is interested. About half of them were prepared in order to perform retrievals of CO<sub>2</sub> densities and to do a subsequent

derivation of hydrostatic temperature profiles. Roughly 40 other orbits show a more complex geometry; still they could be eligible for a similar analysis after modifications to our method for generating radiance vertical profiles, and to perform CO<sub>2</sub> and temperature retrievals. Application of the present inversion scheme to about 50 OMEGA orbits, their analysis and a more extended comparison with global models, is in preparation.

Two improvements of the scheme are foreseen, the extension of the retrievals below 120 km and the joint retrieval of CO<sub>2</sub> and temperature. Extending the retrievals below our current lower limit at 120 km in order to cover the upper mesosphere and the homopause would be very interesting. This is of particular importance for extremely cold atmospheres, where radiances above the noise level concentrate below 140 km. The strong CO<sub>2</sub> second hot ro-vibrational bands which dominate the emission up to 140 km are excited mostly by solar pumping in the fundamental transitions in 2.7 μm. These latter bands become optically thick around 120 km, which makes the dependence of the emission on CO<sub>2</sub> very non-linear in the upper mesosphere. In particular, it requires a detailed analysis of the non-LTE collisional and radiative processes competing among them in the 90–120 km range, and perhaps a tabulation or parameterization of the non-LTE dependence on the CO<sub>2</sub> density (*i.e.*, approximate treatment) in order to simplify the impact of the non-linearities on the calculation of the emerging radiances.

Finally, as a further application, the present scheme can be generalized to include other instruments observing limb emissions on Mars, like the case of PFS on board Mars Express, and the LNO channel of the NOMAD spectrometer on board ExoMars Trace Gas Orbiter.

## Declaration of competing interest

The authors declare that they have no known competing financial interests or personal relationships that could have appeared to influence the work reported in this paper.

## Acknowledgments

This work was conducted as part of the project UPWARDS-633127 under the European Union's Horizon 2020 research and innovation Programme. The IAA team was supported by grant PGC2018-101836-B-100 (MCIU/AEI/FEDER, EU) and by the Spanish MCIU through the 'Center of Excellence Severo Ochoa' award to the IAA/CSIC (SEV-2017-0709). OMEGA data are publicly available via the ESA Planetary Science Archive.

## References

- Adriani, A., Dinelli, B.M., López-Puertas, M., García-Comas, M., Moriconi, M.L., Funke, B., 2011. Distribution of HCN in Titan's atmosphere from non-LTE emission from CASSINI/VIMS observations at 3 μm. *Icarus* 214, 584–595. <https://doi.org/10.1016/j.icarus.2011.04.016>.
- Audouard, J., Poulet, F., Vincendon, M., Bibring, J.-P., Forget, F., Langevin, Y., Gondet, B., May 2014. Mars surface thermal inertia and heterogeneities from OMEGA MEX. *Icarus* 233, 194–213. <https://doi.org/10.1016/j.icarus.2014.01.045>.
- Bellucci, G., Altieri, F., Bibring, J.P., Bonello, G., Langevin, Y., Gondet, B., Poulet, F., 2006. OMEGA/Mars Express: visual channel performances and data reduction techniques. *Planet. Space Sci.* 54, 675–684. <https://doi.org/10.1016/j.pss.2006.03.006>.
- Bibring, J.-P., Soufflot, A., Berthé, M., Langevin, Y., Gondet, B., Drossart, P., Bouyé, M., Combes, M., Puget, P., Semery, A., Bellucci, G., Formisano, V., Moroz, V., Kottsov, V., Bonello, G., Erard, S., Forni, O., Gendrin, A., Manaud, N., Poulet, F., Pouilleau, G., Encrenaz, T., Fouchet, T., Melchiori, R., Altieri, F., Ignatiev, N., Titov, D., Zasova, L., Coradini, A., Capaccioni, F., Cerroni, P., Fonti, S., Mangold, N., Pinet, P., Schmitt, B., Sotin, C., Hauber, E., Hoffmann, H., Jaumann, R., Keller, U., Arvidson, R., Mustard, J., Forget, F., 2004. OMEGA: Observatoire pour la Minéralogie, l'Eau, les Glaces et l'Activité. In: Wilson, A., Chicarro, A. (Eds.), *Mars Express: the Scientific Payload*, pp. 37–49.
- Bonello, G., Pierre Bibring, J., Soufflot, A., Langevin, Y., Gondet, B., Berthé, M., Carabedian, C., Jun 2005. The ground calibration setup of OMEGA and VIRTIS experiments: description and performances. *Planetary and Space Science* 53 (7), 711–728. <https://doi.org/10.1016/j.pss.2005.02.002>.
- Bougher, S.W., Roeten, K.J., Olsen, K., Mahaffy, P.R., Benna, M., Elrod, M., Jain, S.K., Schneider, N.M., Deighan, J., Thiemann, E., Eparvier, F.G., Stiepen, A., Jakosky, B., M., 2017. The structure and variability of Mars dayside thermosphere from MAVEN NGIMS and IUVS measurements: seasonal and solar activity trends in scale heights and temperatures. *J. Geophys. Res. Space Physics* 122 (1), 1296–1313. <https://doi.org/10.1002/2016JA023454> (arXiv:<https://agupubs.onlinelibrary.wiley.com/doi/pdf/10.1002/2016JA023454>).
- England, S.L., Liu, G., Yiğit, E., Mahaffy, P.R., Elrod, M., Benna, M., Nakagawa, H., Terada, N., Jakosky, B., Feb 2017. MAVEN NGIMS observations of atmospheric gravity waves in the Martian thermosphere. *J. Geophys. Res. Space Physics* 122 (2), 2310–2335. <https://doi.org/10.1002/2016JA023475>.
- Evans, J.S., Stevens, M.H., Lumpe, J.D., Schneider, N.M., Stewart, A.I.F., Deighan, J., Jain, S.K., Chaffin, M.S., Crismani, M., Stiepen, A., McClintock, W.E., Holsclaw, G., M., Lefèvre, F., Lo, D.Y., Clarke, J.T., Eparvier, F.G., Thiemann, E.M.B., Chamberlin, P.C., Bougher, S.W., Bell, J.M., Jakosky, B.M., 2015. Retrieval of CO<sub>2</sub> and N<sub>2</sub> in the Martian thermosphere using dayglow observations by IUVS on MAVEN. *GRL* 42 (21), 9040–9049. <https://doi.org/10.1002/2015GL065489>.
- Forget, F., Hourdin, F., Fournier, R., Hourdin, C., Talagrand, O., Collins, M., Lewis, S.R., Read, P.L., Huot, J.-P., Oct 1999. Improved general circulation models of the Martian atmosphere from the surface to above 80 km. *JGR* 104, 24155–24176. <https://doi.org/10.1029/1999JE001025>.
- Formisano, V., Maturilli, A., Giuranna, M., D'Aversa, E., López-Valverde, M.A., 2006. Observations of non-LTE emission at 4 microns with the planetary Fourier spectrometer aboard the Mars Express mission. *Icarus* 182, 51–67. <https://doi.org/10.1016/j.icarus.2005.12.022>.
- Funke, B., López-Puertas, M., García-Comas, M., Stiller, G.P., von Clarmann, T., Höpfner, M., Glathor, N., Grabowski, U., Kellmann, S., Linden, A., 2009. Carbon monoxide distributions from the upper troposphere to the mesosphere inferred from 4.7/μm non-local thermal equilibrium emissions measured by MIPAS on Envisat. *Atmos. Chem. Phys.* 9 (7), 2387–2411. URL: <https://www.atmos-chem-phys.net/9/2387/2009/>. <https://doi.org/10.5194/acp-9-2387-2009>.
- Funke, B., López-Puertas, M., García-Comas, M., Kaufmann, M., Höpfner, M., Stiller, G.P., 2012. GRANADA: a Generic RAdiative traNsfer AnD non-LTE population algorithm. *J. Quant. Spectrosc. Radiat. Transf.* 113, 1771–1817. <https://doi.org/10.1016/j.jqsrt.2012.05.001>.
- García-Comas, M., López-Puertas, M., Funke, B., Dinelli, B., Moriconi, M.L., Adriani, A., Molina, A., Coradini, A., 2011. Analysis of Titan CH<sub>4</sub> 3.3 μm upper atmospheric emission as measured by Cassini/VIMS. *Icarus* 214, 571–583. <https://doi.org/10.1016/j.icarus.2011.03.020>.
- Gilli, G., López-Valverde, M.A., Drossart, P., Piccioni, G., Erard, S., Cardesn-Moinelo, A., 2009. Limb observations of CO<sub>2</sub> and CO non-LTE emissions in the Venus atmosphere by VIRTIS/Venus Express. *J. Geophys. Res.* 114 <https://doi.org/10.1029/2008JE003112>.
- Gilli, G., López-Valverde, M.A., Peralta, J., Bougher, S., Brecht, A., Drossart, P., Piccioni, G., Mar, 2015. Carbon monoxide and temperature in the upper atmosphere of Venus from VIRTIS/Venus Express non-LTE limb measurements. *Icarus* 248, 478–498. <https://doi.org/10.1016/j.icarus.2014.10.047>.
- Gilli, G., Forget, F., Spiga, A., Navarro, T., Montabone, L., Millour, E., 2017. On the impact of non-orographic gravity waves in the LMD Mars global climate model. In: Forget, F., López-Valverde, M.Á., Desjean, M.C., et al. (Eds.), *The Mars Atmosphere: Modelling and Observation*, VI, p. 2104.
- González-Galindo, F., López-Valverde, M.A., Forget, F., García-Comas, M., Millour, E., Montabone, L., 2015. Variability of the Martian thermosphere during eight Martian years as simulated by a ground-to-exosphere global circulation model. *Journal of Geophysical Research (Planets)* 120, 2020–2035. <https://doi.org/10.1002/2015JE004925>.
- Gröller, H., Yelle, R.V., Koskinen, T.T., Montmessin, F., Lacombe, G., Schneider, N.M., Deighan, J., Stewart, A.I.F., Jain, S.K., Chaffin, M.S., Crismani, M.M.J., Stiepen, A., Lefèvre, F., McClintock, W.E., Clarke, J.T., Holsclaw, G.M., Mahaffy, P.R., Bougher, S.W., Jakosky, B.M., 2015. Probing the Martian atmosphere with MAVEN/IUVS stellar occultations. *GRL* 42 (21), 9064–9070. <https://doi.org/10.1002/2015GL065294>.
- Gröller, H., Montmessin, F., Yelle, R.V., Lefèvre, F., Forget, F., Schneider, N.M., Koskinen, T.T., Deighan, J., Jain, S.K., Jun 2018. MAVEN/IUVS stellar occultation measurements of Mars atmospheric structure and composition. *Journal of Geophysical Research (Planets)* 123 (6), 1449–1483. <https://doi.org/10.1029/2017JE005466>.
- Jakosky, B.M., Lin, R.P., Grebowsky, J.M., Luhmann, J.G., Mitchell, D.F., Beutelschies, G., Priser, T., et al., 2015. The Mars Atmosphere and Volatile Evolution (MAVEN) mission. *SSR* 195 (1–4), 3–48. <https://doi.org/10.1007/s11214-015-0139-x>.
- Jouget, D., Poulet, F., Langevin, Y., Bibring, J.-P., Gondet, B., Vincendon, M., Berthe, M., 2009. OMEGA long wavelength channel: data reduction during non-nominal stages. *Planetary and Space Science* 57 (8–9), 1032–1042. <https://doi.org/10.1016/j.pss.2008.07.025>.
- Jurado-Navarro, A.A., 2015. *Retrieval of CO<sub>2</sub> and Collisional Parameters From the MIPAS Spectra in the Earth Atmosphere*. Ph.D. thesis. Universidad de Granada.
- Jurado-Navarro, A.A., López-Puertas, M., Funke, B., García-Comas, M., Gardini, A., González-Galindo, F., Stiller, G.P., von Clarmann, T., Grabowski, U., Linden, A., 2016. Global distribution of CO<sub>2</sub> volume mixing ratio in the middle and upper atmosphere from MIPAS high resolution spectra. *Atmospheric Measurements Techniques* 9 (12), 6081–6100. URL: <https://www.atmos-meas-tech.net/9/6081/2016/>. <https://doi.org/10.5194/amt-9-6081-2016>.
- Kaufmann, M., Gusev, O.A., Grossmann, K.U., Roble, R.G., Hagan, M.E., Hartsough, C., Kuteov, A.A., 2002. The vertical and horizontal distribution of CO<sub>2</sub> densities in the upper mesosphere and lower thermosphere as measured by CRISTA. *J. Geophys. Res.* 107 (D23) <https://doi.org/10.1029/2001JD000704>.

- Levenberg, K., 1944. A method for the solution of certain non-linear problems in least squares. *Q. Appl. Math.* 2, 164–168.
- López-Puertas, M., Taylor, F.W., 2001. Non-LTE Radiative Transfer in the Atmosphere. World Scientific, Singapore.
- López-Valverde, M.A., López-Puertas, M., 1994a. A non-local thermodynamic equilibrium radiative transfer model for infrared emission in the atmosphere of Mars. 2: daytime populations of vibrational levels. *J. Geophys. Res.* 99, 13117–13123. <https://doi.org/10.1029/94JE01091>.
- López-Valverde, M.A., López-Puertas, M., 1994b. A non-local thermodynamic equilibrium radiative transfer model for infrared emissions in the atmosphere of Mars. 1: theoretical basis and nighttime populations of vibrational levels. *J. Geophys. Res.* 99, 13093–13115. <https://doi.org/10.1029/94JE00635>.
- López-Valverde, M.A., López-Puertas, M., Funke, B., Gilli, G., García-Camas, M., Drossart, P., Piccioni, G., Formisano, V., 2011. Modeling the atmospheric limb emission of CO<sub>2</sub> at 4.3 μm in the terrestrial planets. *Planetary and Space Science* 59, 988–998. <https://doi.org/10.1016/j.pss.2010.02.001>.
- López-Valverde, M.A., Montabone, L., Sornig, M., Sonnabend, G., Jan. 2016. On the retrieval of mesospheric winds on Mars and Venus from ground-based observations at 10 μm. *Astrophys. J.* 816, 103. <https://doi.org/10.3847/0004-637X/816/2/103>.
- MacQueen, J., 1967. Some methods for classification and analysis of multivariate observations. In: Proceedings of the Fifth Berkeley Symposium on Mathematical Statistics and Probability, Volume 1: Statistics. University of California Press, Berkeley, Calif., pp. 281–297. URL: <https://projecteuclid.org/euclid.bsmsp/1200512992>.
- Mahieux, A., Vandaele, A.C., Robert, S., Wilquet, V., Drummond, R., Montmessin, F., Bertaux, J.L., Jul. 2012. Densities and temperatures in the Venus mesosphere and lower thermosphere retrieved from SOIR on board Venus Express: carbon dioxide measurements at the Venus terminator. *Journal of Geophysical Research (Planets)* 117, 7001. <https://doi.org/10.1029/2012JE004058>.
- Marquardt, D.W., 1963. An algorithm for least-squares estimation of nonlinear parameters. *J. Soc. Ind. Appl. Math.* 11 (2), 431–441.
- Medvedev, A.S., Yiğit, E., 2012. Thermal effects of internal gravity waves in the Martian upper atmosphere. *GRL* 39 (5), L05201. <https://doi.org/10.1029/2012GL050852>.
- Medvedev, A.S., González-Galindo, F., Yiğit, E., Feofilov, A.G., Forget, F., Hartogh, P., 2015. Cooling of the Martian thermosphere by CO<sub>2</sub> radiation and gravity waves: an intercomparison study with two general circulation models. *Journal of Geophysical Research (Planets)* 120 (5), 913–927. <https://doi.org/10.1002/2015JE004802> (arXiv:1504.05550).
- Mertens, C.J., Russell III, J.M., Mlynczak, M.G., She, C.-Y., Schmidlin, F.J., Goldberg, R. A., López-Puertas, M., Wintersteiner, P.P., Picard, R.H., Winick, J.R., Xu, X., 2009. Kinetic temperature and carbon dioxide from broadband infrared limb emission measurements taken from the TIMED/SABER instrument. *Adv. Space Res.* 43 (1), 15–27. <https://doi.org/10.1016/j.asr.2008.04.017>.
- Peralta, J., López-Valverde, M.A., Gilli, G., Piccialli, A., Jan. 2016. Dayside temperatures in the Venus upper atmosphere from Venus Express/VIRTIS nadir measurements at 4.3 μm. *Astron. Astrophys.* 585, A53. <https://doi.org/10.1051/0004-6361/201527191>.
- Piccialli, A., López-Valverde, M.A., Määttänen, A., González-Galindo, F., Audouard, J., Altieri, F., Forget, F., Drossart, P., Gondet, B., Bibring, J.P., 2016. CO<sub>2</sub> non-LTE limb emissions in Mars' atmosphere as observed by OMEGA/Mars Express. *Journal of Geophysical Research (Planets)* 121, 1066–1086. <https://doi.org/10.1002/2015JE004981>.
- PSA, 2019. European Space Agency's Planetary Science Archive. URL: <https://archives.esac.esa.int/psa/> (online, PSA 5.6.8).
- Rodgers, C.D., 2000. Inverse methods for atmospheric sounding - theory and practice. In: Rodgers, Clive D. (Ed.), *Inverse Methods for Atmospheric Sounding - Theory and Practice*, Series: Series on Atmospheric Oceanic and Planetary Physics, vol. 2. World Scientific Publishing Co. Pte. Ltd., ISBN 9789812813718, p. 2. <https://doi.org/10.1142/9789812813718>
- Roldán, C., López-Valverde, M.A., López-Puertas, M., Edwards, D.P., Sep. 2000. Non-LTE infrared emissions of CO<sub>2</sub> in the atmosphere of Venus. *Icarus* 147, 11–25. <https://doi.org/10.1006/icar.2000.6432>.
- Stepanova, G.I., Shved, G.M., Aug. 1985. Radiation transfer in the 4.3-micron CO<sub>2</sub> band and the 4.7-micron CO band in the atmospheres of Venus and Mars with violation of LTE - populations of vibrational states. *Sov. Astron.* 29, 422.
- Stiller, G., 2002. Sensitivity of trace gas abundances retrievals from infrared limb emission spectra to simplifying approximations in radiative transfer modelling. *J. Quant. Spectrosc. Radiat. Transf.* 72, 249–280. <https://doi.org/10.1006/icar.2000.6432>.
- Terada, N., Leblanc, F., Nakagawa, H., Medvedev, A.S., Yiğit, E., Kuroda, T., Hara, T., England, S.L., Fujiwara, H., Terada, K., Seki, K., Mahaffy, P.R., Elrod, M., Benner, M., Grebowsky, J., Jakosky, B.M., Feb 2017. Global distribution and parameter dependences of gravity wave activity in the Martian upper thermosphere derived from MAVEN/NGIMS observations. *J. Geophys. Res. Space Physics* 122 (2), 2374–2397. <https://doi.org/10.1002/2016JA023476>.
- Theon, J.S., Nordberg, W., 1965. On the Determination of Pressure and Density Profiles From Temperature Profiles in the Atmosphere. National Aeronautics and Space Administration, Technical Note.
- Thiemann, E.M.B., Eparvier, F.G., Bouger, S.W., Dominique, M., Andersson, L., Girazian, Z., Pilinski, M.D., Templeman, B., Jakosky, B.M., 2018. Mars thermospheric variability revealed by MAVEN EUVM solar occultations: structure at aphelion and perihelion and response to EUV forcing. *Journal of Geophysical Research (Planets)* 123 (9), 2248–2269. <https://doi.org/10.1029/2018JE005550> (arXiv:1802.02189).
- Vincendon, M., Audouard, J., Altieri, F., Ody, A., 2015. Mars Express measurements of surface albedo changes over 2004–2010. *Icarus* 251, 145–163. <https://doi.org/10.1016/j.icarus.2014.10.029> (arXiv:1407.2831).
- von Clarmann, T., Ceccherini, S., Doicu, A., Dudhia, A., Funke, B., Grabowski, U., Hilgers, S., Jay, V., Linden, A., López-Puertas, M., Martín-Torres, F.-J., Payne, V., Reburn, J., Ridolfi, M., Schreier, F., Schwarz, G., Siddans, R., Steck, T., 2003a. A blind test retrieval experiment for infrared limb emission spectrometry. *J. Geophys. Res.* 108, 4746. <https://doi.org/10.1029/2003JD003835>.
- von Clarmann, T., Glatthor, N., Grabowski, U., Höpfner, M., Kellmann, S., Kiefer, M., Linden, A., Tsidiu, G.M., Milz, M., Steck, T., Stiller, G.P., Wang, D.Y., Fischer, H., Funke, B., Gil-López, S., López-Puertas, M., 2003b. Retrieval of temperature and tangent altitude pointing from limb emission spectra recorded from space by the Michelson Interferometer for Passive Atmospheric Sounding (MIPAS). *J. Geophys. Res. Atmos.* 108, 4736. <https://doi.org/10.1029/2003JD003602>.
- von Clarmann, T., Degenstein, D.A., Livesey, N.J., Bender, S., Braverman, A., Butz, A., Compernolle, S., Damadeo, R., Dueck, S., Eriksson, P., Funke, B., Johnson, M.C., Kasai, Y., Keppens, A., Kleinert, A., Kramarová, N.A., Laeng, A., Payne, V.H., Rozanov, A., Sato, T.O., Schneider, M., Sheese, P., Sofieva, V., Stiller, G.P., von Savigny, C., Zawada, D., 2019. Estimating and reporting uncertainties in remotely sensed atmospheric composition and temperature. In: Atmospheric Measurement Techniques Discussions 2019, pp. 1–63. URL: <https://www.atmos-meas-tech-discuss.net/amt-2019-350/>. <https://doi.org/10.5194/amt-2019-350>.
- Zurek, R.W., Tolson, R.A., Bouger, S.W., Lugo, R.A., Baird, D.T., Bell, J.M., Jakosky, B. M., Mar 2017. Mars thermosphere as seen in MAVEN accelerometer data. *J. Geophys. Res. Space Physics* 122 (3), 3798–3814. <https://doi.org/10.1002/2016JA023641>.